2(1)

Shahid Chamran University of Ahvaz

Journal of

Hydraulic Structures

Scientific Professional Journal



انجمن هیدرولیک ایران

Summer 2016
Volume 2
Issue 1

JORNAL OF
HYDRAULIC STRUCTURES
SHAHID CHAMRAN UNIVERSITY OF AHVAZ

***Manager**: Prof. Hamid R.Ghafouri*
***Editor-in-chief:** Dr. Ali Haghighi*
***Editorial coordinator:** Dr. Seyed Mohammad Ashrafi*
Department of Civil Engineering, Engineering Faculty, Shahid Chamran University of Ahvaz, Ahvaz, Iran.

Members
Prof. Hossein M. V.Samani
Civil Engineering Department, Shahid Chamran University of Ahvaz, Ahvaz, Iran
Prof. Hamid R. Ghafouri
Civil Engineering Department, Shahid Chamran University of Ahvaz, Ahvaz, Iran
Prof. Mohammad M. Shooshtari
Civil Engineering Department, Shahid Chamran University of Ahvaz, Ahvaz, Iran
Prof. Mahmood S. Bajestan
Hydraulic Structures Department, Shahid Chamran University of Ahvaz, Ahvaz, Iran
Prof. Saeed R. S. Yazdi
Civil Engineering Department, K.N.Toosi University of Technology, Tehran, Iran
Prof. Ahmadreza M. Gharabaghi
Civil Engineering Faculty, Sahand University of Technology, Tabriz, Iran
Prof. Behzad Ataie Ashtiani
Civil Engineering Department, Sharif University of Technology, Tehran, Iran
Prof. Masoud Ghodsian
Faculty of Civil & Environmental Engineering, TarbiatModarres University, Tehran, Iran
Prof. Mahmood Javan
School of Agriculture Shiraz University, Shiraz, Iran
Prof. Javad Farhoudi
Department of Irrigation & Reclamation Engineering University of Tehran, Tehran, Iran
Prof. Mohammad R. Jaefarzadeh
Department of Civil Engineering, Ferdowsi University, Mashhad, Iran
Prof. Nasser Talebbeydokhti
Department of Civil Engineering, Shiraz University, Shiraz, Iran
Dr. Mohammad S. Pakbaz
Civil Engineering Department, Shahid Chamran University of Ahvaz, Ahvaz, Iran
Dr. Massoud Oulapour
Civil Engineering Department, Shahid Chamran University of Ahvaz, Ahvaz, Iran
Dr. Arash Adib
Civil Engeering Department, Shahid Chamran University of Ahvaz, Ahvaz, Iran
Dr. Ali Haghighi
Civil Engineering Department, Shahid Chamran University of Ahvaz, Ahvaz, Iran
Dr. Mojtaba Labibzadeh
Civil Engineering Department, Shahid Chamran University of Ahvaz, Ahvaz, Iran

Shahid Chamran Univeristy of Ahvaz

انجمن هیدرولیک ایران

CONTENTS

VOL II, NO I, SUMMER 2016

II ***Aims and Scope***

01 Riprap sizing for scour protection at river confluence
E. G. Adivi, M. S. Bajestan, J Kermannezhad

12 Experimental Investigation of Rill Creating Hydraulic Conditions in the Marl Rangelands in a Tilting Flume
A. Zoratipour, H. Azadi

27 Experimentally determination of discharge coefficients of Ogee spillway under axial arc condition with convergent lateral walls
J. S. Kazemi, M. Saneie, M. AzhdaryMoghaddam

34 Shape Optimization of an abrupt contraction using numerical streamlining
R. Yousefian, S. F. Saghravani

48 Slope Stability Analysis Using a Self-Adaptive Genetic Algorithm
A.H. Ayati, H.M.V. Samani, A. Haghighi

58 Calculation of Leakage in Water Supply Network Based on Blind Source Separation Theory
J. Gao, S. Qi, J. Nan, J. Li

Aims and Scope

Hydraulic Structure Journal is an interdisciplinary journal which publishes high-quality peer-reviewed articles addressing the latest developments and applied methods **in construction, maintenance, management, and operation policy of Hydraulic Structures.**
The Journal aims at providing an efficient route to fast-track publication, **within 10-12 weeks after manuscript submission**. Manuscripts will be considered for publication in the following categories: **research articles**, **technical notes**, **case reports** and **discussions**.

The general areas covered by the Journal include:

- Technical and methodological advances in application, design/selection, production, modification of construction materials
- Advances in numerical and analytical methods
- Hydro informatics and soft computing
- Hydraulic aspects of hydraulic structures
- Applied surface and subsurface hydrology and hydrometeorology
- Forecasting approaches in water resources engineering
- Economic and social aspects of hydraulic structures
- Uncertainty analysis and risk management in hydraulics and water resources engineering
- Application of Nanotechnology in Hydraulic Structures
- Geotechnics of Hydraulic Structures
- Damage detection techniques

The following might be considered as hydraulic structures:

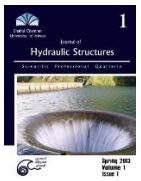
- Dams and associated structures
- River and Watershed Structures
- Offshore and Onshore Structures
- Irrigation and Drainage Channel Networks
- Bridges
- Water Storage and Conveyance Structures
- Pipelines and Pump Stations
- Sewerage Systems
- Water and Wastewater Treatment Plants
- Historical Water Structures

General Information

Title: Journal of Hydraulic Structures
Subject: Hydraulics and water resources engineering
Coverage area: International
Journal Type: Scientific and technical
License Holder: Shahid Chamran University
Editor-in-Chief: Dr. Ali Haghighi
Manager: Prof. Hamid R. Ghafouri
Editorial coordinator: Dr. Seyed Mohammad Ashrafi

Language Editors:
Majid SadollahKhani
Soroosh Kamali
Address: Engineering Faculty, Shahid Chamran University of Ahvaz
Phone #: +986113330010-20 (5610 & 5603)
Fax #: +986113337010
Language: English
Email: jhs@scu.ac.ir
Website: jhs.scu.ac.ir

Journal of Hydraulic Structures
***J. Hydraul. Struct.*, 2016; 2(1): 1-11**
DOI: 10.22055/jhs.2016.12646



Riprap sizing for scour protection at river confluence

Elham Ghanbari Adivi[1]
Mahmood Shafai Bajestan[2]
Jalil Kermannezhad[3]

Abstract

River confluence is a common feature of most irrigation and drainage channels and river systems, where tributary conflicts the main channel. In these section, rapid changes in velocity and discharge, sediment distribution and flow turbulent result in a deep confluence scour, a bar point in the separation zone at downstream of junction corner and finally vortex flow. Thus, the main goal of this study is to conduct a series of experimental tests to investigate the required size of rocks to control the scour hole. The results show that for a constant ratio discharge, Qr, the size of riprap in the incipient motion increases with decreasing in tailwarer depth. In other words, for any rock size the tailwater depth required for incipient motion increases with increasing the ratio of discharge, Qr. For each constant ratio discharge, or, the size of riprap in the incipient motion increases with increasing in tailwater velocity, Vt. Finally, some equations are presented for predicting the size of rocks and the proposed equations has been compared with existing ones.

Keywords: River Confluence, Riprap, Scour hole, Junctions.

Received: 12 December 2015; Accepted: 15 June 2016

1. Introduction

Confluences are the basic building blocks in river networks at all scales. When, two rivers merge at a confluence, rapid changes in fluid velocity and turbulence intensity cause changes in the bed geometry. Usually, a deep scour hole and a depositional point bar are present at the confluence. One important phenomenon that has been overlooked in previous studies is the progressive penetration of the scour hole into the tributary channel. This progressive penetration may jeopardize the structural safety of the lateral channel in the proximity of the main channel. The flow pattern, scour and sedimentation in confluences are complex and have attracted the

[1] Department of Water Science Engineering, Shahrkord University, Shahrkord, 09166077037 Elhamgh44@gmail.com (**Corresponding author**)
[2] Department of Water Science Engineering, Shahid Chamran University, Ahwaz, m-shafai@yahoo.com
3 Department of Water Science Engineering, Lorestan University, Khoram Abad, jalil¬mc2@yahoo.com.com

attention of many researchers. Previous researches on river channel confluences can be classified into two main groups. The first group consists of theoretical and experimental studies focusing on flow characteristic without the inclusion of sediment transport, such as Webber and Greated in 1966 [1], Lin and Soong in 1979 [2], Best and Reid in 1984 [3], Ramamurthy et al. [4], Hager [5], Gurram et al. [6], Hsu et al. [7,8], Bradbrook et al. [9], Lane et al. [10], Weerakoon et al. [11], Biron et al. [12], Weber et al. [13] and Huang et al. [14]. These studies considered parameters such as depth ratio, separation zone dimensions, hydraulic jump conditions or three-dimensional flow effects. The second group includes the analysis of sediment transport (Mosley [15], Best [16], Roy et al. [17], Rhoads and Kenworthy [18], Rhoads and Sukhodolov [19], Bryan and Kuhn [20], Boyer et al. [21], Parsons et al. [22], Ghobadian and Shafai Bejestan [23], Ghobadian [24], Ghanbari Adivi and Shafai Bejestan [25]) Concentrating on confluence scour, sediment transport and bed morphology, effects of bed discordance, shear layer turbulence and mixing. The effects of confluence angle and momentum and discharge ratios have been taken into account in several studies but the effects of tail water depth and bed grain size have received less attention. There is no significant published attempt in the previous studies for developing a relation for predicting the suitable value of stable stone; and this is why the focus of our paper is on this important issue.

These phenomena cause failure in the structure near the confluence area, changes in the river morphology and it causes problem for navigation. Therefore, it has to be made to control the scouring which are the main cause of facing problems. Among the measuring techniques which should be taken into consideration is the use of rocks. Due to three- dimensions of flow and sediment structure at river confluence, investigation on scouring and sedimentation in this area should be possible by physical modeling. Thus the main goal of this study is to conduct a series of experimental tests to investigate the required size of rocks for controlling the scour hole, in other words the purpose of this study is to investigate the factors affecting the stability of the riprap, that used to control erosion at the confluence of the rivers and control sediment transported to the downstream of confluent. To accomplish this goal, over 78 tests were conducted in the flume of the hydraulic laboratory of Shahid Chamran University.

2. Dimensional analysis

In river confluence, many variables can affect the scour hole and point bar dimensions and maximum penetration of scour hole into the tributary channel. To develop a general relation for predicting maximum value of penetration of scour hole into the tributary channel, one may consider the following dependence:

$$f(Q_1, Q_2, Q_3, y_t, y_u, y_b, g, \mu, \rho_w, \sigma, B_1, B_2, B_3, \theta, S_0, n, D_{50}, \rho_s, \phi, F_s, \sigma_g) = 0 \quad (1)$$

In these equations Q1, Q2 and Q3 are flow discharges in the lateral channel and in the main channel upstream and downstream of the confluence, respectively. B1, B2 and B3 are the corresponding channel widths which are equal and constant , θ is the confluence angle, So is the bed slope, both of them are constant.

The riprap is uniform there for the impact of resistance angle φ, geometric standard deviation σg and sediment particle shape factor Fs can be ignored. σ is Surface tension of water.

$$f(Q_1, Q_2, Q_3, y_t, y_u, y_b, g, \mu, \rho_w, \sigma, B, D_{50}, \rho_s) = 0 \quad (2)$$

Applying dimensional analysis, the following non-dimensional equations can be developed

[25].

$$f(F_g, We_3, \mathrm{Re}_3, \frac{Q_2}{Q_1}, \frac{y_t}{y_u}, \frac{y_t}{y_b}, \frac{y_u}{y_b}, \frac{y_t}{D_{50}}, \frac{y_u}{D_{50}}, \frac{y_b}{D_{50}}, \frac{\rho_s}{\rho}) = 0 \quad (3)$$

The depth of flow upstream of the confluence, yu and depth of lateral channels, yb are affected by depth of flow downstream of the confluence, yt ; therefore, yu and yb can be removed. Fg is the densimetric Froude number and Re3 is the Reynolds number downstream of the river confluence. Fg is computed as Vt/[g (Gs-1) D50]0.5, with Vt being the flow velocity downstream of the confluence, g the acceleration of gravity. Gs the specific gravity of the sediment (Gs = ρs/ ρw), D50 the median particle size and ρs density viscosity of sediment, while Re is equal to VtYt ρw/μ with ρw and μ representing density and dynamic viscosity of water, respectively. Considering that stability number (S.N) and Fg show the effect of gravity on the flow hydraulic, But because of the importance of (S.N) in particle stability analysis, Fg can also be disregarded. Weber number downstream of the connection point, We3 is disregarded because Weber in open channel is negligible. All experimental tests in this study have been carried out under subcritical conditions and therefore the bed slope has no significant effects on the flow patterns [6]. For high Reynolds number and rough boundaries, the Reynolds number effect can also be disregarded. Therefore, Eq. 3 is reduced to the following form:

$$S.N = g(Q_2/Q_1 , y_t/D_{50}) \quad (4)$$

Equation 4 is the basis for the analysis of the experimental data.

3. Experimental setup and methodology

The experimental setup consists of a main flume 9 m long with 70 cm deep for the first 2.4 m and 40 cm for remaining 7 m with 35 cm wide and a lateral flume 3 m long, 40 cm deep and either 25 or 35 cm wide. Both flumes had a horizontal slope. At the upstream end of each flume a stilling box was installed to reduce the kinetic energy of the entrance flow.

A head tank provides a constant discharge to both stilling boxes. The amount of Discharge is measured by an electronic flow meter with an accuracy of 0.01 L sec^{-1}. At the end of the main flume, a sluice gate controls the downstream water depth. The lateral flume was connected to the main flume at one confluence angle, i.e., 60°. This study was conducted in hydraulic laboratory at Shahid Chamran University, Ahvaz, Iran during 2011-2012. Figure 1 shows a plan view of the experimental setup. A 7 cm layer of uniform sediment was laid on both channel beds. There was no sediment feeding or recirculation in these experiments. In order to extend the densimetric Froude number range, five different sizes of sediment (D_{50} = 3.53, 7.1, 11.11, 15.87, and 22.22 mm) with *Gs* equal to 2.65 and three different sizes of sediment (D_{50} = 11.11, 15.87 and 22.22 mm) with *Gs* equal to 1.61 (sponge iron) were used. At the start of each run the flumes were filled slowly, keeping the tailwater gate closed. When, the flow depth was high enough to avoid initial disturbances on the bed, the flow discharges were increased to the desired values and the tailwater gate was gradually opened until the desired flow depth was achieved. This situation was kept unchanged for 5 h or until the scour hole dimensions remained constant.

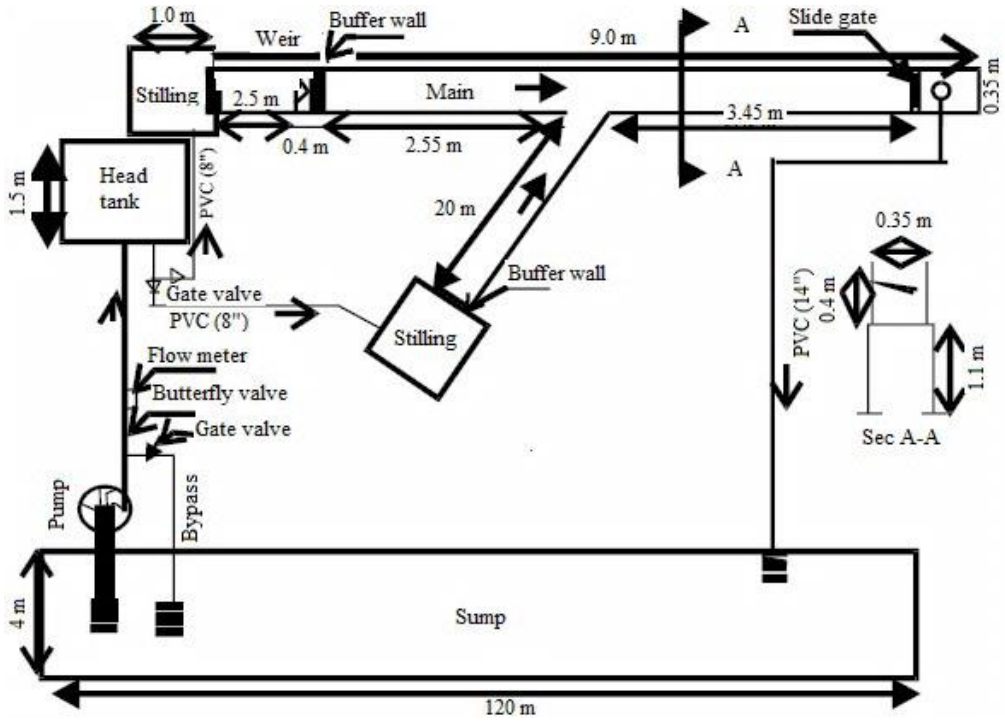


Figure1. Plan view of experimental set up

4. Results and discussion

In this investigation, 78 experiments on stability number were carried out. Table 1 shows the range of the relevant parameters and dimensionless variables covered by the experiments.

Table 1: Range of variables in this study

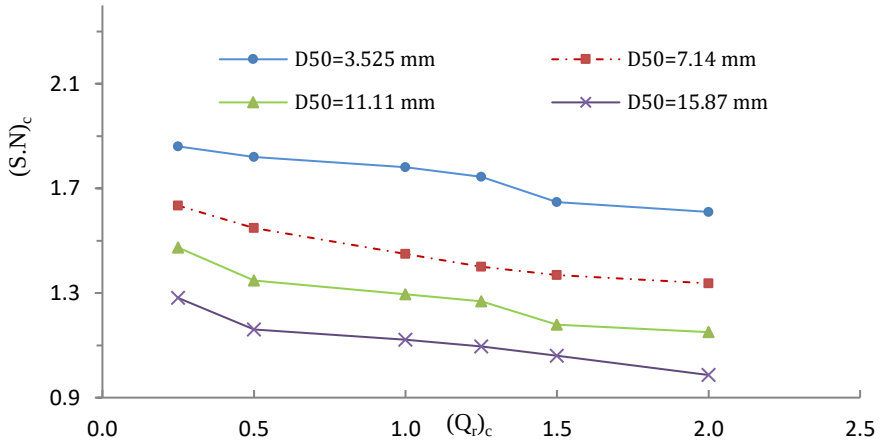
parameter	value
Width (B), cm	35
Confluence angle (θ),deg.	60
Discharge ratio (Q_r)	0.25, 0.5, 1, 1.25, 1.5, 2
Q_t (lit/sec)	25, 30
D_{50} (mm)	3.53, 7.1, 11.11, 15.87, 22.22
G_s(relative density)	2.65, 1.61
Test condition	Threshold , failure

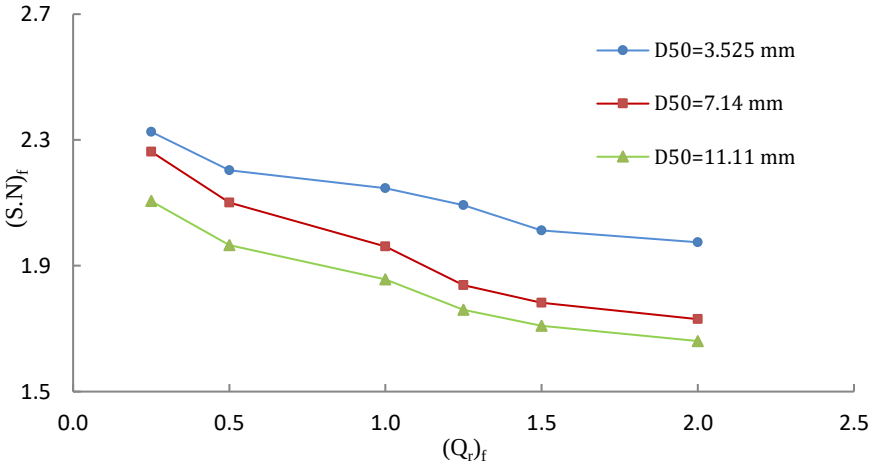
Effect of flow ratio (Q_r) on the stability number (S.N)

One of the parameters that have the highest effect on the stability number is flow rate (Q_r). The results corresponding to 8 sets of the experimental tests are presented in Fig. 2. All other sets showed similar trends. In this study six different discharge ratios $Q_r = Q_2/Q_1$ were analyzed and it can be seen that the discharge ratio significantly effects the bed scouring. As shown in these figures, decreases the stability number with increasing flow rate, for a particle size of riprap. As it increases the flow rate of the main channel before crossing canals, momentum and velocity in the channel increase and the resultant lateral forces that acting on the particles in the bed at confluence,

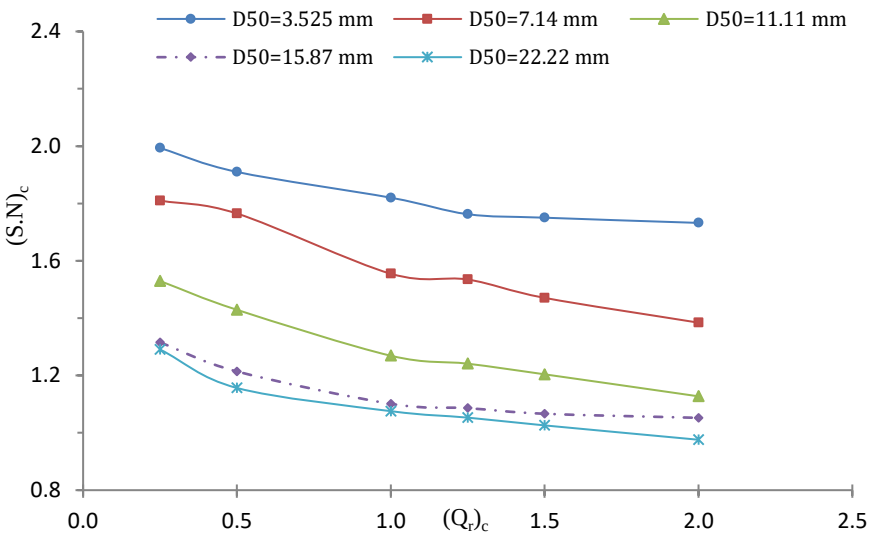
it changes. It has played an important part in the motion of particles. Therefore threshold of particle motion (or failure) occurs at a lower velocity. Based on the relation's stability number, with decreasing at the velocity, the stability number is reduced. It was observed that at the constant flow rate, although there are larger particles, threshold motion is higher but stability number is reduced at this situation.

a : (G_s = 2.65 , Q_t = 25 lit/s)





c : (G_s = 2.65 , Q_t = 30 lit/s)



d : (G_s = 2.65 , Q_t = 30 lit/s)

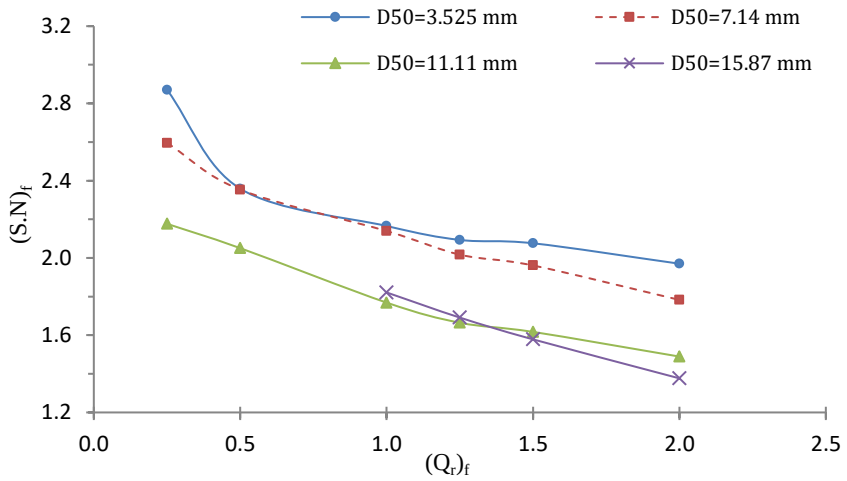


Figure 2 (a-d). Variation of stability number (S.N) with flow rate (Q_r)

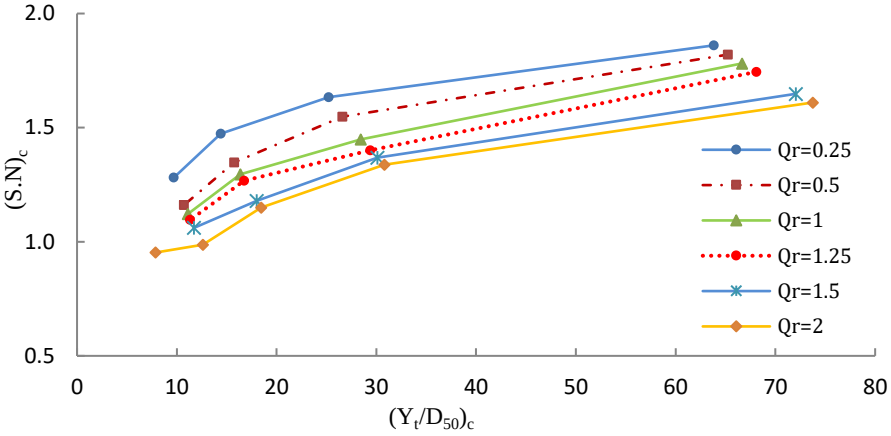
Effect of flow ratio (Y_t/D_{50}) on the stability number (*S.N*)

Rate of tailwater depth to particle size (Y_t/D_{50}), is one of the another parameter that affects on stability number in both threshold and failure condition.

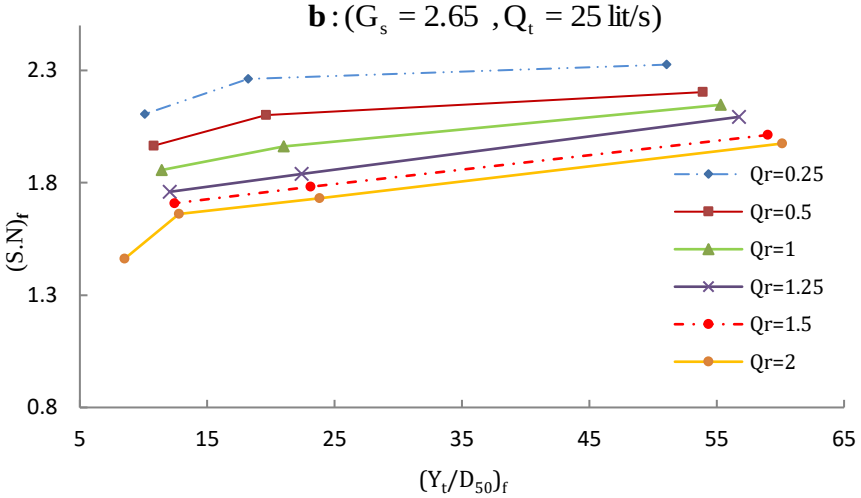
According to these figures (3: a-f) at a constant flow ratio, with increasing (Y_t/D_{50}) (proportional to the decrease in particle diameter) stability number is enhanced, because with reducing the particle diameter the resistance force due to the weight and threshold motion of it is reduced but, Because of the particle diameter decreases, observed that the threshold velocity of the particle diameter (stability number) is decreasing in this situation. This trend results from a decrease in the momentum of the lateral channel when the flow ratio decreases (all other

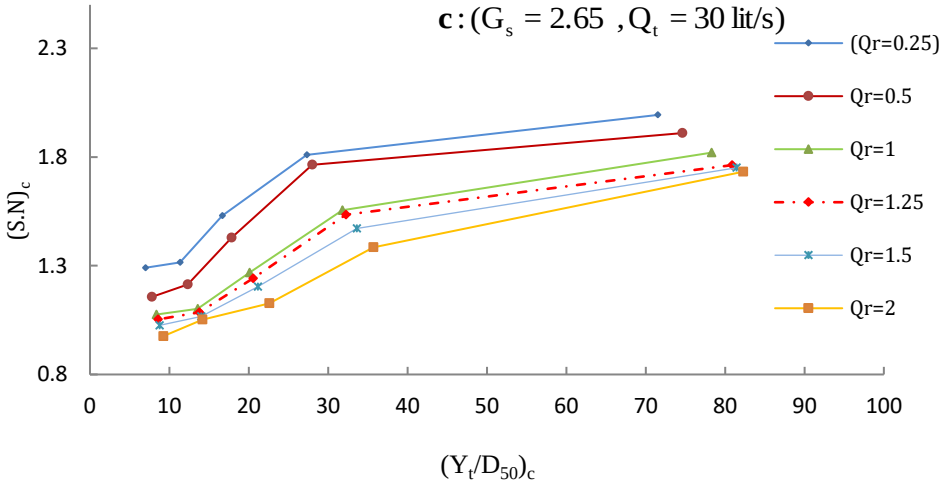
parameters being constant) and then increases at stability number.

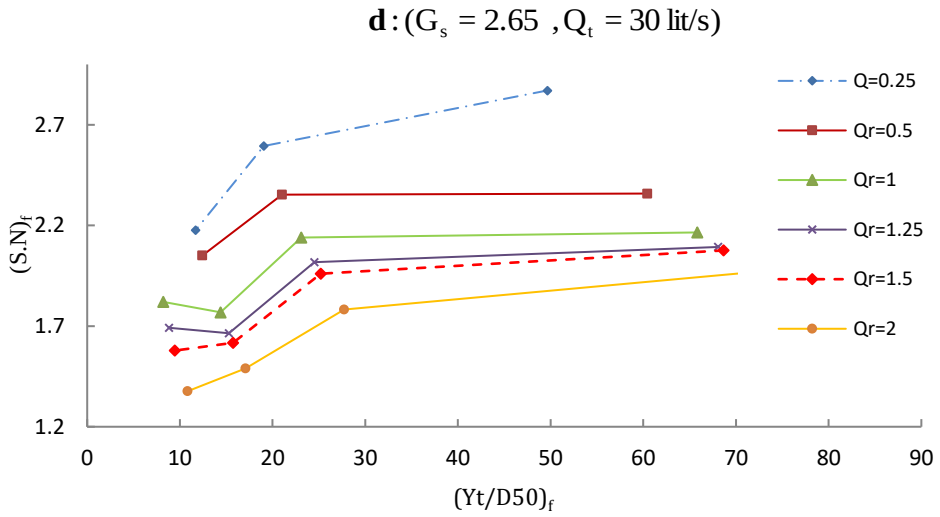
a : (G_s = 2.65 , Q_t = 25 lit/s)

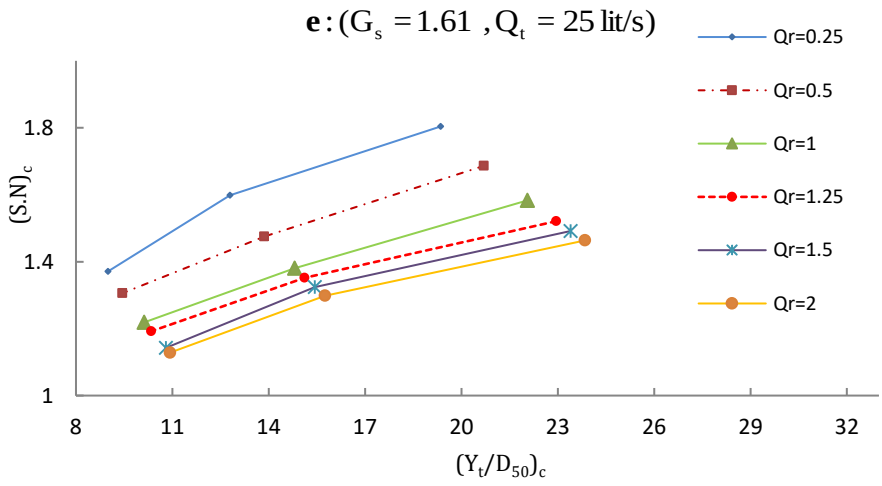


b : (G_s = 2.65 , Q_t = 25 lit/s)




c : (G_s = 2.65 , Q_t = 30 lit/s)
(Qr=0.25)
Qr=0.5
Qr=1
Qr=1.25
Qr=1.5
Qr=2
(S.N)_c
(Y_t/D_50)_c


d : (G_s = 2.65 , Q_t = 30 lit/s)
Q=0.25
Qr=0.5
Qr=1
Qr=1.25
Qr=1.5
Qr=2
(S.N)_f
(Yt/D50)_f


e : (G_s = 1.61 , Q_t = 25 lit/s)
Qr=0.25
Qr=0.5
Qr=1
Qr=1.25
Qr=1.5
Qr=2
(S.N)_c
(Y_t/D_50)_c

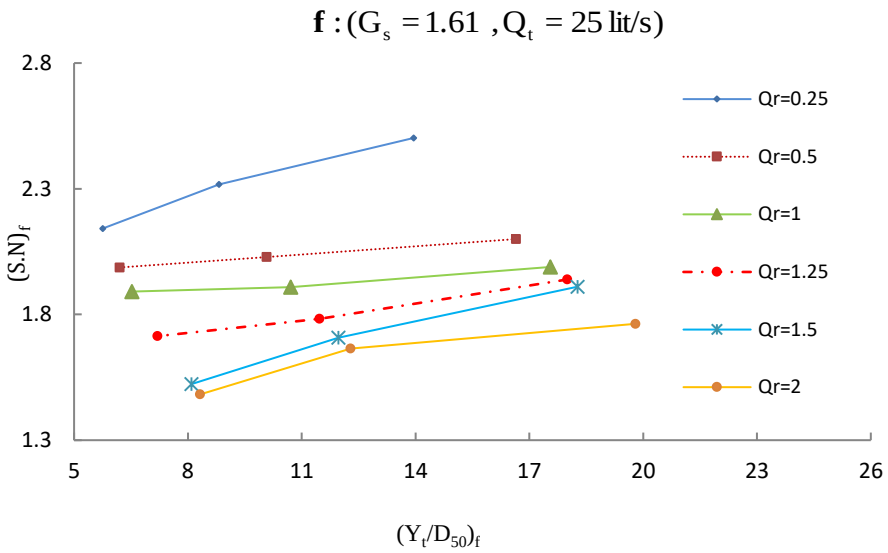


Figure 3 (a-f). Variation of stability number (S.N) with rate of tailwater depth to particle size (Y_t/D_{50})

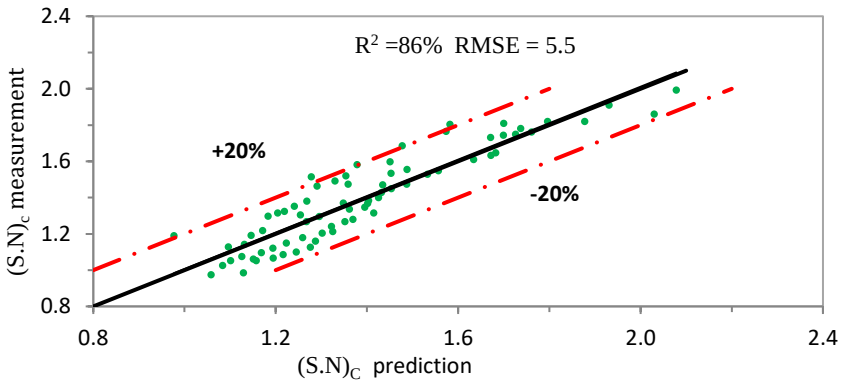


Fig. 4: Observed values of stability number of riprap at the channel confluence versus predicted values by Eq. 5

Stability number equation

To develop a relation to predict the maximum particle size of stable riprap into the tributary channel at the river confluences, the following equation was obtained by multiple regressions on the experimental data (r = 86%):

$$(S.N)_c = 0.722(Y_t/D_{50})_c^{0.209}.(Q_r)_c^{(-0.119)} \quad (5)$$

The range of applicability of Eq. 5 is given by the values of Table 1 and it must be noted that it is valid only when there is no movement of bed material upstream of the channel confluence.

In order to investigate the accuracy of Eq. 5, the observed values of relative stability number have been plotted against the predicted values and the results are presented in Fig. 4. As it can be seen from this figure most of data are between the 80% confidence bands statistical analyses. The relative error of the equation is about 14%. This means that Eq. 5 can be applied as a guide in the prediction of maximum size of stable riprap into the tributary channel at river confluences. The form of Eq. 5 clearly shows that the flow ratio has a negative effect while the other parameters (Y_t/D_{50}), have positive effect on the relative stability of riprap particle.

5. Conclusion

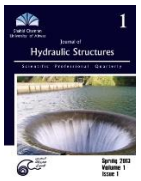
In this study a general dimensionless equation for the prediction of maximum particle size of stable riprap into the tributary channel at river confluences has been developed. A series of 78 experimental tests with constant confluence angle and width at both channels, and also different discharge ratio (Q_r) and relative density (G_s) in an asymmetrical confluence have been conducted to test the proposed formulation. The results showed that the stability number of riprap into the tributary channel increases with increasing the ratio of tailwater depth to particle size (Y_t/D_{50}); while it decreases with increasing the ratio of lateral channel discharge to main channel discharge at upstream of the confluence. A relationship has also been introduced that has a 14% relative error for predicting stable particle diameter of riprap into the tributary channel.

References

1. N.B. Webber, and C.A. Greated, 1966. An investigation of flow behavior at the junction of rectangular channel. Proc. Instn. Civ. Engres., 34: 321-334.
2. J.D. Lin and H.K. Soong, 1979. Junction losses in open-channel flows. Water Resour. Res., 15: 414-418.
3. J.L. Best and I. Reid, 1984. Separation zone at open-channel junctions. J. Hydraulic Eng., 110: 1588-1594.
4. A.S. Ramamurthy, L.B. Carballada and D.M. Tran, 1988. Combining open channel flow at right angled junctions. J. Hydraulic Eng., 114: 1449-1460.
5. W.H. Hager, 1989. Transition flow in channel junctions. J. Hydraulic Eng., 115: 243-259.
6. S.K. Gurram, K.S. Karki and W.H. Hager, 1997. Subcritical junction folw. J. Hydraulic Eng. ASCE, 123: 447-455.
7. C.C. Hsu, F.S. Wu and W.L. Lee, 1998. Flow at 90 equal-width open-channel junction. J. Hydraulic Eng. ASCE, 124: 186-191.
8. C.C. Hsu, W.J. Lee and C.H. Chang, 1998. Subcritical open-channel junction flow. J. Hydraulic Eng. ASCE, 124: 847-855.
9. K.F. Bradbrook, P.M. Biron, S.N. Lane, K.S. Richards and A.G. Roy, 1998. Investigation of controls on secondary circulation in a simple confluence geometry using a three-dimensional numerical model. Hydrol. Processes, 12: 1371-1396.
10. S.N. Lane, K.F. Bradbrook, K.S. Richards, P.A. Biron and A.G. Roy, 1999. The application of computational fluid dynamics to natural river channels: Three-dimensional versus two-dimensional approaches. Geomorphology, 29: 1-20.

11. S.B. Weerakoon, Y. Kawahara and N. Tamai, 1991. Three-dimensional flow structure in channel confluences of rectangular section. Proceedings of 24th Congress of International Association for Hydraulic Research, September 1991, Madrid, Spain, pp: 373-380.
12. P.M. Biron, A. Richer, D.A. Kirkbride, G.A. Roy and S. Han, 2002. Spatial patterns of topography at a river confluence. Earth Surf. Processes Land Forms, 28: 913-928.
13. L.J. Weber, E.D. Schumate and N. Mawer, 2001. Experimentals on flow at a 90° open-channel Junction. J. Hydraulic Eng. ASCE, 127: 340-350.
14. J.L. Huang, L.J. Weber and G.L. Yong, 2002. Three-Dimensional numerical study of flows in open-channel junctions flow. J. Hydr. Engrg., 128: 268-280.
15. M.P. Mosley, 1976. An experimental study of channel confluences. J. Geol., 85: 535-562.
16. J.L. Best, 1988. Sediment transport and bed morphology at river channel confluences. Sedimentology, 35: 481-498.
17. A.G. Roy, R. Roy and N. Bergeron, 1988. Hydraulic geometry and changes in flow velocity at a river confluence with coarse bed material. Earth Surface Processes Land forms, 13: 583-598.
18. B.L. Rhoads and S.T. Kenworthy, 1998. Time-averaged flow structure in the central region of a stream confluence. Earth Surface Processes Landforms, 23: 171-191.
19. B.L. Rhoads and A.N. Sukhodolov, 2001. Field investigation of three-dimensional flow structure at stream confluences: 1.Thermal mixing and time-averaged velocities. Water Resour. Res., 37: 2393-2410.
20. R.B. Bryan, and N.J. Kuhn, 2002. Hydraulic conditions in experimental rill confluences and scour in erodible soils. Water Resour. Res., 38: 1-22.
21. C. Boyer, A.G. Roy and J.L. Best, 2006. Dynamics of a river channel confluence with discordant beds: Flow turbulence, bed load sediment transport and bed morphology. J. Geophys. Res., 111: F04-F04.
22. D.R. Parsons, J.L. Best, S.N. Lane, O. Orfeo, J.R. Hrady and R. Kostaschuk, 2007. Form roughness and the absence of secondary flow in a large confluence-diffluence rio parana, argentina. Earth Surface Processes Landforms, 32: 155-162.
23. R. Ghobadian, and M. Shafai Bejestan, 2007. Investigation of sediment patterns at river confluence. J. Applied Sci., 7: 1372-1380.
24. R. Ghobadian, 2007. Investigation of flow, scouring and sedimentation at river-channel confluences. Ph.D. Thesis, Department of Hydraulic Structures, Shahid Chamran University, Ahwaz, Iran.
25. E. Ghanbari Adivi, M. Shafai Bajestan and M. Saghi, 2013. Laboratory study of stability in the riprap materials of bed at the confluence of rivers. J. Water and soil Sci. 24: 43-58.

Journal of Hydraulic Structures
***J. Hydraul. Struct.*, 2016; 2(1):12-26**
DOI: 10.22055/jhs.2016.12647



Experimental Investigation of Rill Creating Hydraulic Conditions in the Marl Rangelands in a Tilting Flume

Amin Zoratipour[1]
Hossein Azadi[2]

Abstract

Generally, the evaluation and assessment of the critical condition of rill formation are useful for a better understanding of soil erosion processes. The inherence characteristics of soils, which have much dynamic variations on the hillslopes and are affected by rill formation, are the soil critical shear stress and soil erodibility factors. This study aims to assess experimental rill incision thresholds, the determined soil critical shear and soil erodibility factors on marl formation based on precipitation characteristics and different slope gradients on sensitive marl soil. The results showed that the rainfall intensity and slope steepness factors separately and together can significantly affect the distance from the point of rill initiation; runoff and rill start time and soil loss values. Rainfall intensity showed more importance than the slope gradient in the point of rill formation. There is a significant relationship between rainfall intensity and slope gradient with rill incision point, time of runoff start and rill start and soil loss. The point of rills formation (slope length) decreases with an increase in slope gradient and rainfall intensity. Finally, the results revealed that the values of soil erodibility factor (Kr) and critical shear stress of marl soil are 0.0015s m^{-1} and 0.267N m^{-2}, respectively.

Keywords: Critical shear stress, soil erosion rate, rainfall intensity, slope gradient, marl

Received: 25 December 2015; Accepted: 15 April 2016

1. Introduction

Most of previous studies show that rain-impacted flows are largely responsible for erosion in rill and interrill erosion areas (Kinnell, 2005). Generally, the mechanisms of soil erosion by splash, interrill and rill erosion are water erosion sub-processes which have different mechanisms (Govers et al., 1986). Interrill erosion and rill erosion are the two basic types of soil erosion in agricultural catchments in Iran. When a rainstorm event occurs, both commonly coexist on steep slopes,

[1] Assistant Professor, Ramin Agriculture and Natural Resources Uni., zoratipor@yahoo.com (**Corresponding author**)
[2]Assistant Professor, Scientific Staff of Gent Uni.

especially in the marl areas of Iran. The rill formation process includes three stages: detachment, entrainment, and the transport of soil particles driven by concentrated surface water. Rill erosion is the second stage of the erosion dynamic process in catchments, which is a function of soil erodibility factor, soil hydraulic transfer capacity and flow shear stress (Kinnell et al., 2005). Rills are characterized as an incised channel that is at least 5 cm length, 0.5 cm deep, and 1 to 2 cm wide (Torri et al., 1987). After creation, the rills expanded the upstream and downstream of hill-slopes (Toy et al., 2002). According to Horton's (1945) threshold theory, the rate at which soil particles are detached can be related to the amount by which one of the flow hydraulics variables such as flow stress shear, stream power and unit discharge, characterizing the hydraulics of the flow, exceeds a critical soil specific value (Knapen et al., 2007). Some studies indicate that soil erosion resistance to the concentrated flow is influenced by almost any soil property. In other words, rill incision begins when overland flow shear stress exceeds soil critical shear stress. Obviously, the expanding of rills depends on some parameters such as water shear force (flow shear stress) and soil resistance. Therefore, soil erosion made by the concentrated flow is highly dependent on flow conditions and soil interior characteristics such as critical shear stress. When the overland flow reaches a critical point (the point at which soil particles lose the ability to remain in place and are detached by flowing water), a rill starts to form. Although studies (Romero et al., 2007; Zhang et al., 2008) on concentrated flows and rill formation processes have mainly focused on small plots, and only a single rill; studies with larger plots that allow observations of groups of rills would lead to more generalized conclusions are rill initially being formed on a hillslope (Toy et al., 2002). Yao et al., (2008) carried out a study related to the critical shear stress on an eroding rill to slope steepness and discharge on silty-clay soil from the Loess Plateau in China in a large sloping indoor plot (8m×3m) with five different slope gradients using simulated rainfall at three rainfall intensities. He observed that slope was rather more important than rainfall intensity in determining the location of the rill initiation. The range of soil critical shear stress in his study was determined from 1.33 to 2.63 Pa. The soil critical shear stress was also inversely related to the slope gradient and not influenced by the rainfall intensity.

Generally, the marl formation field is one of the important sensitive soils to rill and gully erosions and also is the most sediment resource in the Iran that gives a high priority to be studied (Ahmadi, 1999). Given only few studies have been conducted on knowing the dynamic variations of rill erosion in marl degraded lands in general, and especially in Iran, the general goal of this study is to realize the dynamic variations of rill erosion degraded rangelands on marl in the country. Considering the lack of temporal and spatial reliable quantitative information in the scale of each rill, the study assesses the temporal and spatial thresholds of rill formation and soil loss values in marl degraded rangelands of Iran. Furthermore, the study estimates the critical shear stress and soil erodibility factors in the laboratory flume.

2. Material and methods

Study area

The study was carried out in the Taleghan watershed, a midstream tributary of the Sefid Roud basin in the north of Iran (Fig. 1). The watershed is located between 36° 5′ 17″ and 36° 20′ 45″ N and 50° 39′ 33″ and 51° 11′ 26″ E, and ranges in elevation from 1852 to 4100 m. According to the FAO (1993) classification, the climate is semi-arid and the average annual precipitation at the Taleghan station is 480 mm. The total area of the basin is 1243km^2.

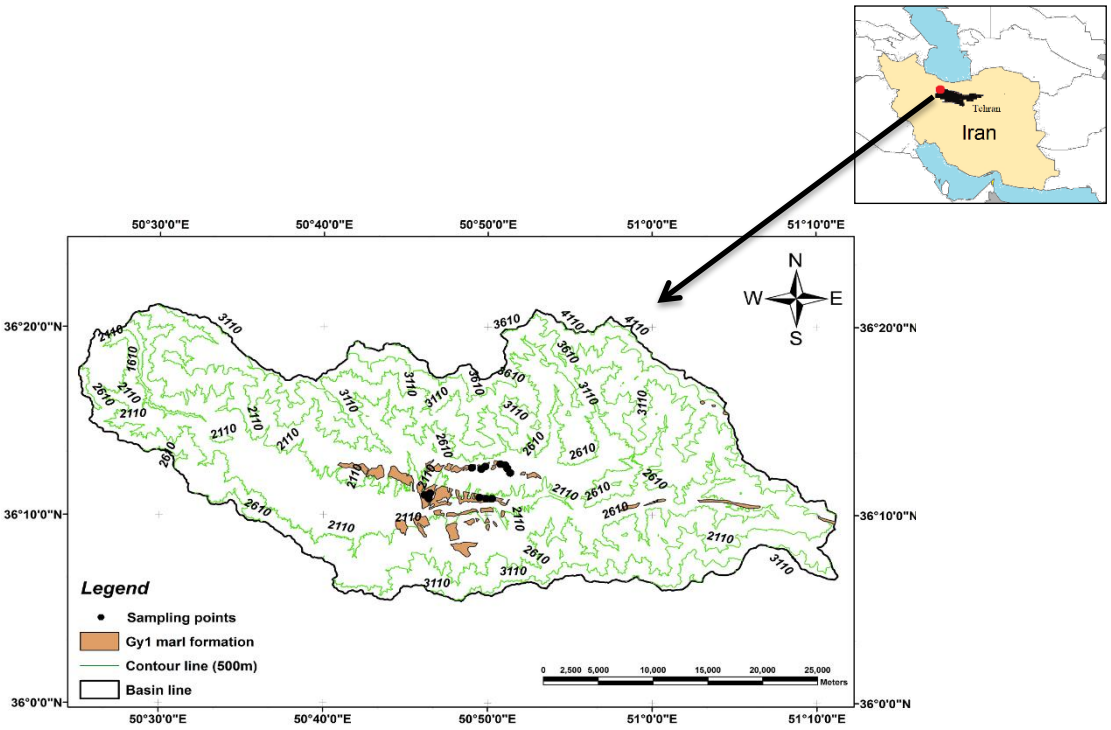


Fig.1.The location of the Taleghan watershed in Iran and the location of sampled points of the marl formation

Marl formations and marl sub-layers cover about 25-30 million ha of Iran's area (Soil Conservation and Watershed Management Research Center of Iran, 2005). The saline-gypsum marl formations cover a wide area of lands in arid and semi-arid regions of Iran. Marl formation consists of different classes on the base physical and chemical properties soil particles, which includes: Ngc, Ngm, Gy_1 and Gy_2 marls (Ahmadi, 2006). According to some studies (Ahmadi, 1999), the Gy_1 and Gy_2 marl formations, due to the presence of gypsum and salt materials, are more erodible than rest of marl formations, as the thickness of this formation is estimated approximately 200-300 meters. These formations are one of the greatest sources of the country's sediment, with a high degree of erodibility. In away Gy_1 saline-gypsum formation has decreased the effective longevity of huge dams in Iran such as Sefidroud and Taleghan Glinak (Ahmadi, 2006). Erosion processes in this kind of marl are active and include different forms of erosion such as, interrill, sheet, rill, gully, piping and badland formation. It should be noted that the vegetation cover at marl areas is low and it has a sparse distribution (Ahmadi, 1999) that shows the rill and interrill erosion in degraded rangelands of the Taleghan watershed are common (Fig. 2). Table 1 shows that the soil of the case study has a clay texture. It also shows the physical and chemical properties of the marl soil in different points (12 points) of the Taleghan basin.



Fig.2.Rill and interrill area in degraded lands of the Taleghan basin

Table 1.The average of some physical and chemical properties* of the marl soil of the study area used in the rainfall-erosion simulate

Characteristic	*Average*	*S.d. (±)***	*Characteristic*	*Average*	*S.d. (±)*
Sand	*6%*	*1.7*	*pH*	*7.9*	*0.05*
Silt	*38%*	*3.3*	*EC*	*0.26(dS m^{-1})*	*0.01*
Clay	*56%*	*2.9*	*Gypsum*	*11.3%*	*1.7*
Bulk density	*1.4(g cm^{-3})*	*0.03*	*$CaCo_3$*	*19.2%*	*2.1*
Porosity	*46.2%*	*4.9*	*Saturation*	*42.2%*	*4.2*
Organic matter content	*0.45%*	*0.13*	*Stones and pebbles*	*8.5%*	*2.5*

* The soil texture was defined by USDA (1991), Bulk density is performed with clod method (Blake and Hartge; 1986), Organic matter content by Nelson and Sommers (1982), EC and pH by Kiniry et al. (1983), Gypsum, CaCo3, Saturation and Porosity by Klute (1986); Page et al. (1982). ***S.d.: Standard deviation.*

Experimental setup

The experiment was conducted in a (1m×6m) tilting flume in the laboratory at the Institute of Soil Conservation and Watershed Management Research, Iran. The flume has advantages such as pressurized water, rainfall plane 7.75 m above the flume level, changeable slope up to 60% and the capability of intensity regulation (10-125 mm/h). At the preparation stage of the experimental flume, after transporting the soil from the field to the experimental site, the soil was air-dried. The clods in the soil were broken up, and the soil was sieved with a 10 mm screen. A 15 cm layer of gravel particles was uniformly placed in the bottom of the plot box as drainage layer. On the top of the gravel layer, a marl soil was packed loosely and evenly by a depth of 25 cm. The soil used in this experiment was obtained from the root layer (50 cm top soil level) of degraded marl rangelands in the Taleghan watershed (Fig.1). A protective thick gauze cloth was located between gravel particles and marl soil surface. During the packing process, a static weight method was used to compact the soil uniformly in the box (Yao et al., 2008). After packing the flume of soil and

compacting it layer by layer with a homogeneous cylinder, the soil surface was smoothed manually with a rake. Then, the plot was prepared in a horizontal position and the flume soil was saturated from the below surface of the flume. After the soil saturation, to let the soil become equilibrated, it was left for at least 24 h, such that the surplus water came out of outlet drainage. Thus, the plot remained in a horizontal position to ensure a uniform and homogeneous initial soil moisture profile (Yao et al., 2008). In the beginning of each experiment, before performing the simulated rainfall, the bulk density test is determined randomly from the compacted soil (superficial and deep samplers), such that the bulk density of the compacted soil complied with the bulk density of field conditions. The same action was performed in other experiments.

Using the curves of rainfall intensity-duration-frequency from the Taleghan Synoptic station, this study first evaluated the rainfall distribution. The distribution was selected of rainfall with return periods of 2, 25, and 100 years. Then, the selected rainfalls were generated and calibrated by the rainfall simulator to simulate the erosion-rainfall process. So, the simulation of erosion-rainfall process at the intensities of 10, 55 and 110 (mm h^{-1}) presents the intensity of rainfall at the return periods of 2, 25 and 100 years, respectively. A large runoff plot (1m×6m) was used with a rainfall simulator (Fig. 3). The plot rested on a platform that was adjustable to two slope gradient (22.17% and 44.63%). To measure the position of the rill initiation during the experiment, the rulers were fixed on the metal borders of the plot, and the entire plot surface was divided into 6 blocks (1 m^2 each). The soil was packed in the plot to a bulk density of 1.4 g cm^{-3} for every layer. The treatments included two slope gradients 22.17% and 46.63%, each with a three-level of rainfall intensity (10, 55, and 110 mm h^{-1}) and they were carried out in two repetitions. These ranges for the slope gradient and rainfall intensity were selected to cover the storm and field conditions observed in the Taleghan basin. In this study, the ranges were selected as erosion critical conditions on the Gy_1 marl formation in Taleghan. Finally, 12 different treatments on the bases of the slope steepness and rainfall intensities were simulated.

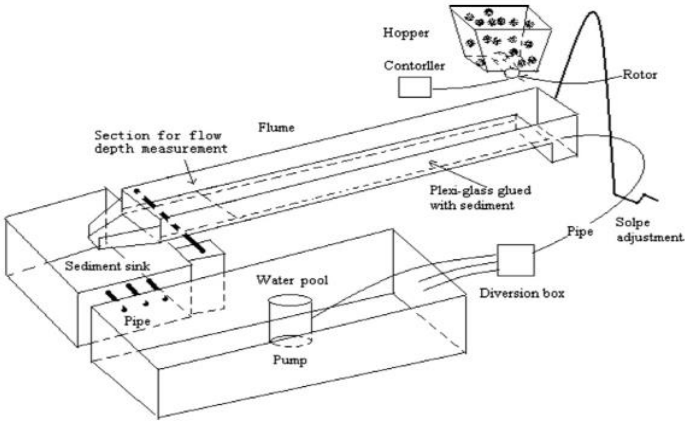


Fig.3. Schematic diagram of experimental set-up of the tilting flume

Experimental Procedure

Following the soil preparation, every experiment was performed 24 h after the initial saturation. At the initial stage of each experiment, the flume was set at the desired slope gradient and rainfall intensity. In each test, the starting time of the simulated rainfall, the time when runoff reached the outlet of the plot, and the time when rill initiation occurred were recorded. In each experiment,

sediment samples together with runoff were taken every minute for about 30 minutes after the start of the runoff. The runoff discharge, runoff volume, and sediment concentration were measured at the outlet of the test plot for different rainfall intensities and slope gradients. During the experiments, the flow velocity was measured by the dye tracing technique (potassium permanganate) and also using a stopwatch to record the time required for the dye to travel a given distance (Yao et al., 2008). The flow velocities were measured by recording the travel time of the dye cloud over a distance of 1 m. The average travel time was taken as the mean of 5 measurements (each 6-minute, one time) (Cao et al., 2009). The runoff samples were allowed to settle overnight to separate the suspended sediments from water in the samples. The remaining water and sediment were transferred into containers that were dried in ovens at 105°C for more than 24h, or until the samples got completely dry. Then, the mass of the sediment was measured and used to calculate the sediment concentration. In addition, the distance from the top of the plot to the point of initiation was measured; the median distance of all rills in a test was used in subsequent calculations as length to the rill initiation (Yao et al., 2008). During each experiment, the distance from the top of the plot to the point of rill initiation, time of runoff start and time of rill start on the soil surface were measured.

Data analysis

According to Cao et al., (2009), the critical conditions of rill incision relates to hydraulic parameters of the surface water flow and soil inherence characteristics. In this regard, Yao et al. (2008) explained that the critical point of rill incision is a small pit that is created on the plot or hillslope during the experiment and then develops into a rill. Accordingly, two important parameters for the rill initiation are considered as the flow shear stress and soil erodibility coefficient. Several approaches are used in different studies to estimate flow hydraulic parameters such as shear stress, stream power and the determination of soil detachment in rills. The hydraulic shear stress; τ (Pa), on the bases equations of simple force-balance for uniform flow depth, can be derived from Cao et al., (2009):

$$\tau = \rho\, g\, h_i\, S \tag{1}$$

where τ (Pa) is the shear stress, ρ (kg m^{-3}) is the water mass density, g (m s^{-2}) is the gravity constant, h (m) is the flow depth, and S is the tangent value of slope gradient. Also, the flow depth at the above equation was calculated by the following equation (Yao et al., 2008):

$$h = \frac{q}{V} \tag{2}$$

where h (m) is the flow mean depth, q (m^2 s^{-1}) is the unit flow discharge at the outlet point and V (m s^{-1}) is the flow mean velocity on the hillslope. Also, the stream power (ω) can be calculated from the equation (3), as Cao et al. (2009):

$$\omega = \tau V = \rho\, g\, h\, S\, V \tag{3}$$

where ω (kg m^{-3}) is the stream power, V (m s^{-1}) is the mean flow velocity. According to Knapen et al. (2007), in the case of predicting soil detachment from simple hydraulic indicators, there are several basic models to predict soil detachment which use the main hydraulic variables that control soil detachments such as slope gradient, flow velocity, flow depth and the hydraulic roughness

factor to the measured soil loss. Different studies have presented the two models according to threshold concept to predict the rill detachment capacity; one is used for the excess shear stress models and the other excess stream power models. In order to predict the rill detachment capacity on the base of excess shear stress model, the general form of this equation is used, as shown in the equation (4) (Govers et al., 2007):

$$D_c = K\,(a\tau - \tau_c)^b \quad (4)$$

where D_c is the amount of sediment detached per unit of bed surface per unit of time (kg m^{-2} s^{-1}), K is soil erodibility factor (s m^{-1}), τ is the shear stress of the flow (N m^{-2}), τ_c is the critical shear stress of soil (N m^{-2}), a and b are constants. It should be mentioned that K, a, b and τ_c are determined empirically. In most cases, the constants a and b are assumed equal to unity or close to unity (e.g., b =1.05) (Govers et al., 2007, p. 89). The rill erosion rate (D_r) per plot could be calculated from the erosion rate per rill, multiplied by the number of rills, and divided by the plot area (Sheridan et al., 2000). Generally, the soil detachment rate is defined as the soil loss of per square meter per second. In this study, the rate was calculated as the total mass of soil loss (original oven-dry mass minus final oven-dry mass) divided by the time interval of the test and the cross-section area of the soil sample (Cao et al., 2009). The following rill detachment equation was applied to calculate K_r values (Romero et al., 2007; Govers, et al., 2007):

$$D_c = K_r\,(\tau - \tau_c) \quad (5)$$

where D_c = rill detachment capacity for clean water (kg m^{-2} s^{-1}); K_r = rill erodibility (s m^{-1}); τ_c = the shear below when there is no detachment or critical shear stress (Pa); τ = hydraulic shear stress of flowing water (Pa); $\tau = \gamma rs$, where γ = specific weight of water = 9810 N m^{-3}; r = hydraulic radius of rill, m; and s = hydraulic gradient of rill flow). In this paper, the rill erodibility parameters K_r and τ_c are determined experimentally from the measured erosion rates at a range of flow shear values. The measured rill detachment values (kg m^{-2} s^{-1}) were plotted against the hydraulic shear (Pa) values. The slope of the regression line is K_r, and the intercept with the horizontal axis is the critical shear, τ_c. Lastly, the critical slope length to the rill initiation is defined as the distance from the top of the plot to the point where a rill began to form which each test was determined (Sheridan et al., 2000; Knapen et al., 2007). Also, in this study, Change Rate factor (Cr) was used to determine sensitive variables in soil erosion between slope steepness and rainfall intensity at different treatments. This factor shows the sensitive analysis quantitatively, i.e. the amount of change in interval to rill incision to the upside of the flume in different slope gradients and rainfall intensities. The general form of this relationship is defined in the equation (6) (Yao et al., 2008):

$$cr = \frac{\Delta L_i}{L_o} \times 100 \quad (6)$$

Where cr is the change rate (%) of interval of rill initiation, ΔL_i is the change range of slope length to the rill incision from one treatment to another, and L_0 is the slope length to rill incision of 22.17% slope gradient in different rainfall intensities or that of 10 mm h^{-1} rainfall intensity in different slopes.

3. Results

Relationships between hydraulic parameters

Table 2, presents the flow unit discharges, flow mean velocity, flow depth, and flow shear stress for each treatment. According to the results of the table, the shear stress can range from 0.217 to 2.075 Pa. Also, the results showed that the increased flow discharge leads to an increase in the flow depth and followed by an increase in the flow shear stresses.

Fig. 4 shows a linear regression between shear stress changes and the rate of rill detachment in all the simulation tests. Thus, the values of marl soil erodibilty factor Gy_1 (K_r) and critical shear stress of marl soil can directly be estimated by using the rainfall simulator (line slope and intercept of the graph represents (Kr) and (τ) values respectively). Finally, according to the results, the values of marl soil erodibilty factor (K_r) and the critical shear stress of marl soil Gy_1 are 0.0015 (s m^{-1}) and 0.267 (N m^{-2}), respectively.

Sensitivity Analysis

The results average of all the observations for a given experiment that was calculated as the slope length to the rill initiation (Figs 5 to 7). In addition, Table 3 shows the results of reaching time of the runoff at the plot outlet as the runoff start threshold, the start time of rill incision as rill formation threshold, and the total amount of soil loss in each treatment. Sensitivity analysis of results shows that the slope length of rill initiation has a greater sensitivity to rainfall intensity than to slope gradient. According to the results of the table 2, the impact of rainfall intensity on the slope length to rill initiation is more significant than that of the slope steepness: 36.1% versus 13.6% within the tested range.

Results of variance analyses and means comparison variables

Variance analysis

To study the significance of the investigated factors on the studied variables, an analysis of variance was performed using SAS software (version 9.1). Table 2 and Figs. 5-7 show the results of variance analyses of different variables, also means comparison in different categories. The results indicate high significant ($P \leq 0.01$) differences for the slope gradient and intensity in all the studied variables (Table 2). Also apart from the rill incision point, the ANOVA estimation showed that the interaction effects between slope and intensity were significant in the rest of variables.

Results of means comparison: Runoff start time and rill start time

The obtained means of the studied factors and their corresponding interaction of each variable were separately subjected to the Tukey test that uses the studentized range statistic to make all of the pairwise comparisons between groups (McHugh et al., 2007). The averages of the runoff start time in the three selected levels of the rainfall intensity (10, 55 and110 mm h^{-1}) were realized differently (Fig. 5a). The lowest intensity significantly shows the highest runoff start time compared to the two others (11'30" vs. 2'30" and 1'25"). Also, the averages of the runoff start time in the two selected levels of the slope gradient (22.17 and 44.63%) were realized dissimilar as

Table2. Hydraulic parameters of rainfall-induced surface flow

Test	*Rainfall intensity (mm/h)*	*Slope gradient (%)*	*Repetition*	*Flow unit discharge (m^2/s)*	*Mean flow velocity (m/s)*	*Mean flow depth ($m\times10^{-3}$)*	*Flow shear stress (N/m^2)*
1	10	22	1	0.0000413	0.073	0. 566	0.2430
2	10	22	2	0.0000365	0.078	0. 467	0.2168
3	10	44	1	0.0001842	0.125	1.473	0.3425
4	10	44	2	0.000241	0.12	2.008	0.4673
5	55	22	1	0.00031	0.143	2.200	1.0379
6	55	22	2	0.00029	0.161	1.809	0.9420
7	55	44	1	0.00112	0.196	5.702	1.6334
8	55	44	2	0.000872	0.191	4.564	1.2286
9	110	22	1	0.000422	0.204	2.066	0.9758
10	110	22	2	0.000495	0.203	2.442	1.1587
11	110	44	1	0.002337	0.27	8.653	2.0745
12	110	44	2	0.0017	0.29	5.843	1.4174

Table3. Results of variance analysis of the variables Runoff start time, Rill start time, Rill incision point and soil loss between treatments

	Runoff start time	***Rill start time***	***Rill incision point***	***Soil loss***
	M.S	***M.S***	***M.S***	***M.S***
Slope gradient	*38.9***	*25.23***	*0.65**	*1.055***
Rain fall intensity	*123.3***	*125.26***	*5.9***	*18.57***
Interaction	*28.83***	*12.93**	*0.243^{ns}*	*0.83***
CV%	*18.8*	*18.16*	*6.1*	*12.94*

** Significant at the level of 0.05($P \leq 0.05$) ** Significant at the level of 0.01 ($P \leq 0.01$), ns, nor significant, M.S.: mean squares*

shown in Fig. 5b. The lowest slope significantly shows the highest runoff start time compared to the other (6'35" vs. 3'20"). Furthermore, the interaction effects of the two factors (rainfall intensity

and slope gradient) were estimated in Fig. 5c. As shown in the figure, the averages of the runoff start time in the lowest intensity are significantly different compared to the two others in the slope level of 22% (16' 25" vs. 2' 45" and 1'40" respectively). According to the figure, the averages of the runoff start time in the other slope level (44%) are similar to the slope gradient 22% in the three rainfall intensities (6' 40" vs. 2' 15" and 1'15" respectively).

Also for the variable rill start time (in the same figure), the averages of the rill start time of the three selected levels of the rainfall intensity (10, 55 and110 mm h^{-1}) were recognized dissimilar (Fig. 5a). The lowest intensity significantly shows the highest rill start time compared to the two others (12'35" vs. 4'15" and 1'25"). Furthermore, the averages of the rill start time of the two selected levels of the slope gradients (22 and 44%) were recognized differently (Fig. 5b). The lowest slope gradient significantly shows the highest rill start time compared to the other (7'40" vs. 4'45"). Also, the interaction effects of the two factors (rainfall intensity and slope) in Fig. 4c shows that the averages of the rill start time are significantly different in the slope level of 22% in the three rainfall intensities (16'5", 4'45" and 2'15"). According to the figure, the averages of the rill start time in the other slope level (44%) in the lowest intensity are significantly different compared to the two others (9'00" vs. 3'45" and 1'30"). Consequently, the lowest levels of both intensity show the highest rill start time (16'5" in 10 mm h^{-1} and 9'00" in 110 mm h^{-1}). In other words, the highest levels of intensity show the lowest rill start time (Fig. 5c).

Results of means comparison: Rill incision point

With regards to the variable rill incision point, according to Fig. 6a, the averages of the rill incision point in the three selected levels of the rainfall intensity (10, 55 and110 mm h^{-1}) were found differently. The three selected levels of the rainfall intensity factor show significant difference compared to the others (5.65m, 4.1m and 3.25m). The averages of the rill incision point of the two selected levels of the slope gradient (22 and 44%) were realized similarly as shown in Fig. 5b (4.57m vs. 4.1m). Furthermore, the interaction effects of the two factors (rainfall intensity and slope gradient) estimated in Fig. 6c shows that the averages of the rill incision point are significantly different in the slope level of 22% in the three rainfall intensities (6m , 4.05m and 3.65m). According to the figure, the averages of the rill incision point are significant in the other slope level (44%) in the three rainfall intensities (5.3, 4.15 and 2.85m). In addition, the lowest levels of intensity and slope gradient factors (10 mm/h and 22%) showed the highest interval of rill incision point until upper end flume (6 m). Thus, the highest levels of intensity and slope gradient factors show the lowest the interval rill incision point to the upper flume (2.85 meter) (Fig. 6c).

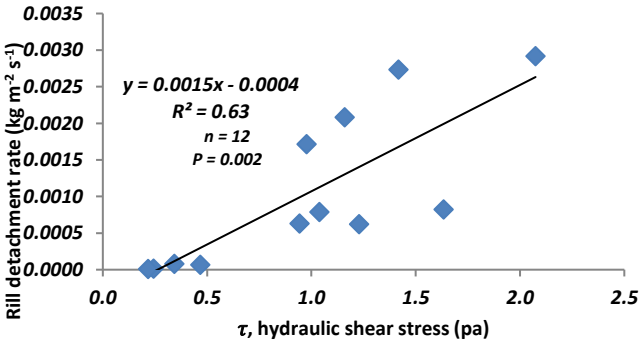


Fig. 4. Rill detachment rate on marl soil as a function of hydraulic shear stress (τ)

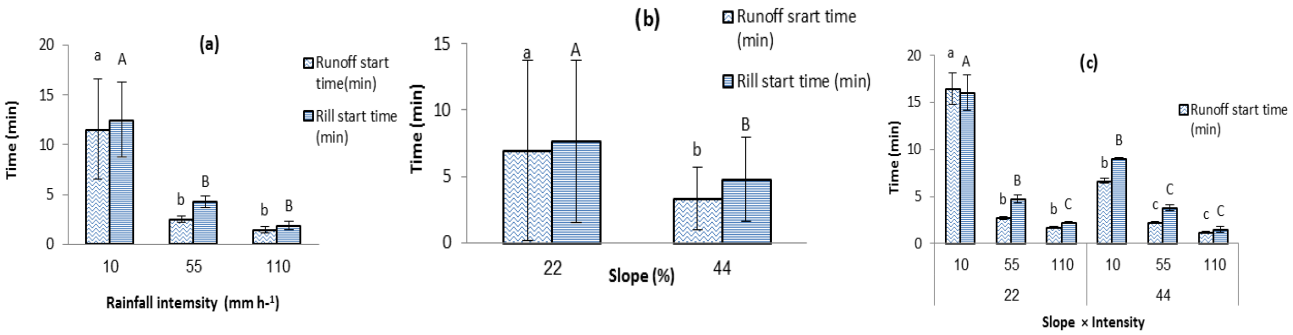


Fig.5. Runoff start time and Rill start time as a function of (a) Rainfall intensity, (b) Slope gradient and (c) Slope gradient × rainfall intensity. Common letters show non-significant mean (estimated by Tukey, P 0.05), n = 12.

Results of means comparison: Rate of soil loss

As demonstrated in Fig.7a, the averages of the rate of soil loss in the three selected levels of the rainfall intensity (10, 55 and110 mm h^{-1}) in 30 minutes rainfall, were verified differently. The highest intensity (110 mm h^{-1}) significantly shows the highest rate of soil loss compared to the two others. The three selected levels of the rainfall intensity (10, 55 and110 mm h^{-1}) were determined differently. The three selected levels of rainfall intensity factor show significant difference (0.075 kg m^{-2}, 1.29 kg m^{-2} and 4.26 kg m^{-2}). Also, the averages of the soil loss of the two selected levels of the slope (22 and 44%) were realized similar as shown in Fig. 7b. The lowest slope significantly shows the lowest soil loss compared to the other (1.55kg m^{-2} vs. 2.2 kg m^{-2}). Furthermore, the interaction effects of the two factors (rainfall intensity and slope gradient) were estimated in Fig. 7c. As shown in the figure, the averages of the soil loss are significantly different in the slope level of 44% in the three rainfall intensities (0.131 kg m^{-2}, 1.3 kg m^{-2} and 5.085 kg m^{-2}, respectively). Also, according to the figure, the averages of the soil loss are significant in the other slope level (22%) in the three rainfall intensities (0.0185 kg m^{-2}, 1.275 kg m^{-2} and 3.44 kg m^{-2}, respectively). According to the above means tests, we found out that increasing the slope gradient and rainfall intensity will induce a decrease in the runoff start time but also a decrease in the rill incision time and rill incision point. While the inverse trend can be observed as the increased soil loss (from left to right in Fig. 7c, increasing the slope gradient and rainfall intensity may lead to an increase in the soil loss. Therefore, increasing the slope gradient and rainfall intensity can direct a decrease in the runoff start time, rill incision time, and slope length of rill incision but an increase in the soil loss.

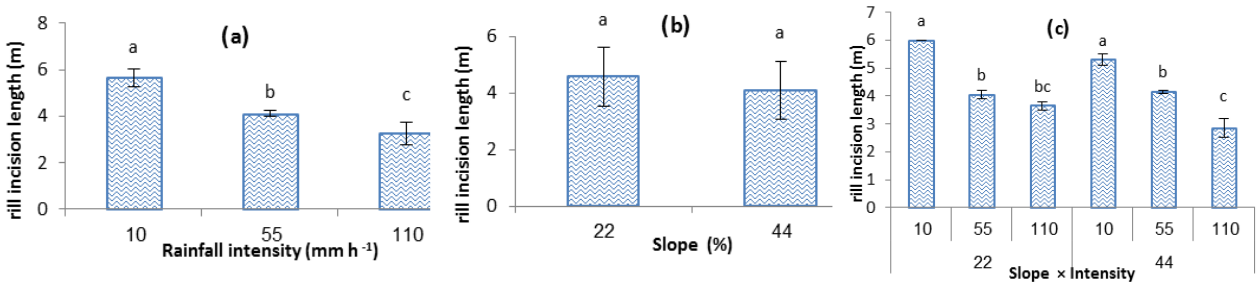


Fig.6. Rill incision point as a function of (a) Rainfall intensity, (b) Slope gradient and

(c) Slope gradient × rainfall intensity, Common letters show non-significant mean (estimated by Tukey, P≤ 0.05), n = 12.

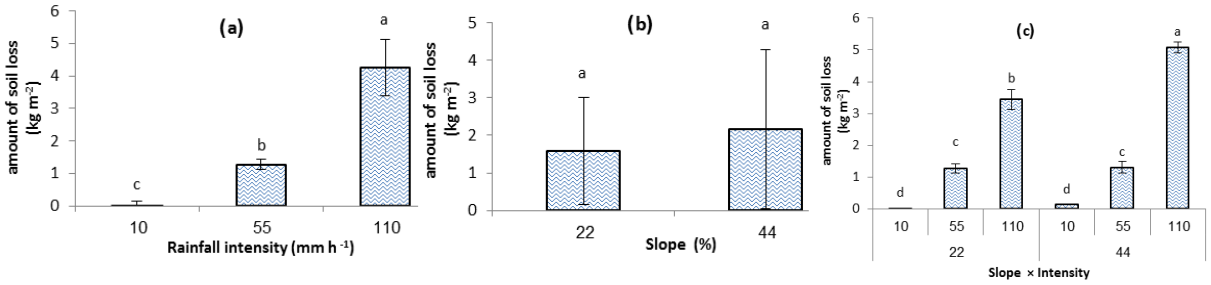


Fig.7. Soil loss as a function of (a) Rainfall intensity, (b) Slope gradient and

(c) Slope gradient × rainfall intensity; in 30 min, Common letters show non-significant mean (estimated by Tukey, P≤ 0.05), n = 12.

It can be explained that once each rill incision is formed, it will be extended to upper end of the flume. In other words, the formation of rill erosion develops with increasing the rainfall intensity and slope gradient toward upper end of the flume. During each test, the surface runoff that was available to initiate rill formation at the upstream end of the rills was limited. So the upward movement of rill head cut from the rill incision point was not significant compared with the development of the rills downslope of the point of rill initiation.

It was also determined that in the first test (i.e. rainfall intensity of 10 mm/h and slope of 22% treatment in two repetitions) did not create rill erosion during the 30 minutes precipitation. Moreover, in constant with the rainfall intensity, the increasing slope gradient will increase soil loss exponentially. As shown in Fig.7, this increasing was estimated about 6 times in low intensity (10 mm/h) and about 50 percent in high intensity (110 mm/h). According to Fig.7c, the maximum amount of the soil loss in rainfall intensity is estimated at 110 mm/h intensity whereas the minimum is 10 mm/h intensity (4.27 and 0.075 kg m^{-2} in 30 min, respectively). The results also showed that the rill incision time threshold decreases with an increase in rainfall intensity and slope gradient (Fig.7). In other words, by increasing rainfall intensity, the rill formation time reduces in relation with the start of precipitation. This means that the rills are formed in a shorter

time than before and develops toward the upside of the flume. The results of the runoff time threshold were similar to rill incision time threshold, although with different rates.

4. Discussion

The results of this study are comparable with some other investigations conducted under other conditions. For example, Yao et al. (2008) studied silty loess soils and reported a shear stress range from 1.33 to 2.63 Pa. Also, Shainberg et al., (1996) used an arable soil and determined the shear stress range from 0.79 to 1.72 Pa. Govers et al., (2007) determined the values of the soil detachment rate (per unit length) versus shear stress force (per unit length) at the slopes ranging from 0.0398 to 0.22 and discharges ranging from 5.55 (10^{-5} m^3 s^{-1}) to 6.1 (10^{-4} m^3 s^{-1}) for a silt loam soil. They also determined the shear stress and detachment rate factors' range, from 0.1 to 4.1 (kg s^{-2}) and 0 to 0.08 (kg s^{-1} m^{-1}), respectively. Persyn et al., (2005) carried out a study on the Biosolids (subsoil and top soil) which determined the shear stress range from 2.70 to 9.80 Pa for unvegetated soil and range from 4.5 to 13.00 Pa for vegetated soil. Romero et al. (2007) studied the measurement of rill erodibility factor (K_r) and concluded that K_r values can range from 0.3 to 19 × 10^{-3} s m^{-1}. Despite differences in soil type and plot size, the critical shear stress values obtained in this study were within other ranges found in other reports.

The values of marl soil erodibilty factor (K_r) and critical shear stress of marl soil Gy_1 are estimated 0.0015 s m^{-1} and 0.267 Nm^{-2}, respectively. These values are in agreement with the results of other studies such as Govers et al., (2007), Yao et al., (2008), Romero et al., (2007) and Mahmoodabadi et al., (2007). Noticeably, the parameters represent different quantities and both are needed for the measurement of erosion rates by concentrated flow in the other regions.

5. Conclusion

This paper analyzed the spatial and temporal variations of the rill formation on the hillslopes of Gy_1 marl formations that is poorly studied in Iran and available literature. The results on the rill incision (spatial and temporal) significantly demonstrated a clear downward trend of the rill incision point, runoff start time, rill start time and an upward trend of soil loss by increasing rainfall intensity and slope gradient. The study also showed a significant correlation between the rainfall intensity and slope gradient which both can affect the rill incision point, runoff start time, rill start time and the amount of soil loss. Although the rainfall intensity and slope steepness both affect the distance from the top of the plot to the point of rill initiation (slope length), rainfall intensity is found more important than the slope in the point of rill formation. In other words, the impact of rainfall intensity on the slope length of rill initiation was more significant than that of the slope. It was also proved that these parameters (slope gradient and rainfall intensity) are related with the variations of rill incision both spatially and temporary. The spatial and temporal thresholds of the rill incision have a diminishing trend with increasing slope gradient and rainfall intensity. Obviously, explaining the temporal and spatial variation in soil erosion resistance simply based on one soil property is not possible. Also, according to the measured value of marl soil erodibility, marl soil will have high sensitivity against the concentrated flows and high ability to create rill erosion on the slope ranges from 20 to 45 %. Finally, this study helps to predict and estimate the amount of soil loss per rainfall incident in a given area and also to estimate the economic value of the loss in different regions with different topography. All this can help decision makers to estimate the sustainability of a watershed more effectively.

6. Acknowledgment

The author wish to thank the Institute of Soil Conservation and Watershed Management

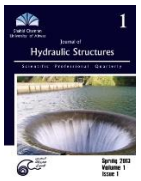
Research Center of Iran (ISCWM) which provided the facilities to conduct this study at the tilt flume in the simulated rainfall and erosion laboratory. Also, i wish to thank of Prof. Yan Nyssen, Prof. Frank Witlox and Dr. Hossein Azadi (Department of Geography, Gent University) for their great support during the last stages of this study.

References

1. H. Ahmadi, 1999. The applied geomorphology: water erosion vol.1, 3th ed. Tehran University, Tehran. [In Persian]
2. M. Arabkhedri, 2008. Study on Rain Characteristics and Calibration of Rainfall Simulator of Soil Conservation and Watershed Management Research Center. Final Report on 83013-0000-01-040000-003-2 Project. Institute of Soil Conservation and Watershed Management Research, Tehran. [In Persian]
3. L. Cao, K. Zhang, and W. Zhang, 2009. Detachment of road surface soil by flowing water. Catena 76, 155–162.
4. D.L. Corwin, S.M. Lesch, J.D. Oster, and S.R. Kafka, 2008. Short-term sustainability of drainage water reuse: spatio-temporal impacts on soil chemical properties. Environmental Quality 37, 8-24.
5. R.G. Foster, D.C. Flanagan, M.A. Nearing, L.J. Lane, L.M. Risse, and S.C. Finkner, 1995. Water Erosion Prediction Project (WEPP). Technical documentation. NSERL Report No.10. National Soil Erosion Research Laboratory. USDA-ARS-MWA.1196 SOIL Building. West Lafayette, IN 47907-1196.
6. G. Govers, R. Giménez, and K. Van Oost, 2007. Rill erosion: Exploring the relationship between experiment modelling and field observations. Earth Science Reviews 84, 87–102.
7. G. Govers, 1990. Empirical relationships for the transport capacity of overland flow in erosion, transport and deposition Processes. IAHS 189, 45-63.
8. G. Govers, 1992. Relationship between discharge, velocity and flow area for rills eroding loose, non-layered materials. Journal of Earth Surface Processes and Landforms 17(5), 515-528.
9. J.W Hummel, K.A. Sudduth, and S.E. Hollinger, 2001. Soil moisture and organic matter prediction of surface and subsurface soils using an NIR soil sensor. Computers and Electronics in Agriculture 32, 149–165.
10. A. Knapen, J. Poesen, G. Govers, G.Gyssels, J. Nachtergaele, 2007. Resistance of soils to concentrated flow erosion: A review. Earth Science Reviews 80, 75-109.
11. P.I.A. Kinnell, 2005. Raindrop-impact-induced erosion processes and prediction: A review. Hydrology Process 19, 2815-2844.
12. O.V. McHugh, T. Steenhuis, B. Abebe, and M. Fernandes, 2007. Performance of in situ rainwater conservation tillage techniques on dry spell mitigation and erosion control in the drought-prone North Wello zone of the Ethiopian highlands. Soil and Tillage Research 97, 19-36.
13. J. Nachtergaele, j. Poesen, 2002. Spatial and temporal variations in resistance of loess derived soils to ephemeral gully erosion. European Journal of Soil Science 53, 449–463.

14. M.A.Nearing, G.R. Foster, L.J. Lane, and S.C. Finkner, 1999. A process-based soil erosion model for USDA Water Erosion Prediction Project technology. Trans. ASAE 32(5), 1587-1593.
15. R.A. Persyn, T.D. Glanville, T.L. Richard, J.M. Laflen, and P.M.Dixon, 2005. Environmental effects of applying composted organics to new highway embankments: Part III Rill erosion. Trans ASAE 48(5), 1765-1772.
16. J. Poesen, s.F. Ingelmo and H. Mucher, 1990. The hydrological response of soil surfaces to rainfall as affected by cover and position of rock fragments in the top layer. Earth Surf Process Landforms 15, 653–671.
17. C. Romero, L. Stroosnijder, and G.A. Baigorria, 2007. Interrill and rill erodibility in the northern Andean Highlands. Catena 70, 105–113.
18. S.H. Schoenholtz, H. Van Miegroet, and J.A. Burger, 2000. A review of chemical and physical properties as indicators of forest soil quality: challenges and opportunities. Forest Ecology and Management 138, 335-356.
19. I. Shainberg, D. Goldstein, and G.J. Levy, 1996. Rill erosion dependence on soil water content, aging and temperature. Journal of SSSA 60(3), 916-922.
20. G.J. Sheridan, H.B. So, R.J. Loch, C. Pocknee, and C.M.Walker, 2000. Use of laboratory scale rill and interrill erodibility measurements for the prediction of hillslope scale erosion on rehabilitated coal mine soils and overburdens. Australian Journal of Soil Research 38, 285–297.
21. Soil Conservation and Watershed Management Research Center of Iran, 2005. The countenance of Iran's watersheds. The final report of forest range and watersheds management organization. Institute of Soil Conservation and Watershed Management Research, Tehran. [In Persian]
22. H.L. Throop, S.R. Archer, H.C. Mongerc, and S. Waltman, 2012. When bulk density methods matter: Implications for estimating soil organic carbon pools in rocky soils. Arid Environments 77, 66-71.
23. D. Torri, M. Sfalaga, and M. Del Sette, 1987. Splash detachment: Runoff depth and soil cohesion. Catena 14, 149-155.
24. T.J. Toy, G.R. Foster, and K.G. Renard, 2002. Soil erosion processes, prediction measurement under simulated rainfall. Journal of Soil Science 150, 787-798.
25. C. Yao, T. Lei, W.J. Elliot, D.K. McCool, J. Zhao, and S. Chen, 2008. Critical condition for rill initiation. Tran. ASABE 51(1), 107-114.
26. Q. Zhang, T. Lei, and J.Zhao, 2008. Estimation of the detachment rate in eroding rills in flume experiments using an REE tracing method. Geoderma 147, 8-15.

Journal of Hydraulic Structures
***J. Hydraul. Struct.*, 2016; 2(1):27-33**
DOI: 10.22055/jhs.2016.12648



Experimentally determination of discharge coefficients of Ogee spillway under axial arc condition with convergent lateral walls

Jalal SheikhKazemi [1]
Mojtaba Saneie[2]
Mehdi AzhdaryMoghaddam[3]

Abstract

A dam spillway is a hydraulic structure that appropriately and safely diverts the outflow to downstream, so that the dam stability and passing of flood flows can be guaranteed. Compared to straight crest spillway, an Ogee spillway with curvature in plan in a fixed-width can pass more flow. Therefore under the low hydraulic heads and the need for a smaller place in plane, they are considered as an economical structure so that their application from several aspects are under developed. An experimental model of the Garmi-Chay Miane dam spillway was made in 1:50 scale. The water head over spillway crest was measured in the eight discharges values and consequently the efficiency of spillway were determined. For Q/Qd ranging from 0.63-1.13, discharge coefficient had ascendant trend with acceptable agreement against the diagram of USBR, while for Q/Qd between 1.13-1.51, due to the submergence of spillway, the discharge coefficient decreased.

Keywords: Convergent lateral walls, Curvature in the plan, Discharge Coefficient, Ogee Spillway, Physical modeling

Received: 14 February 2016; Accepted: 23 June 2016

1. Introduction

The capacity of a spillway largely implies the length of spillway and the form of crest. The spillway with curvature in plane has some advantages over structures compare to straightforward spillway. Spillway with curvature in plan provides increased length of crest by fixed wide, thereby the capacity of upstream head increase. The result of the increase of capacity is that it has lower

[1]M.Sc. Hydraulic Structure Engineering, Faculty of Civil Engineering, University of Sistan & Baluchestan, Zahedan, Iran, Phone: +989119926249; E-mail: j.kazemi65@gmail.com (**Corresponding author**)
[2]Associate Professor, Soil Conservation Watershed Management Research Institute (SCWMRI), Tehran, Iran, E-mail: Saneie_m@scwmri.ac.ir
[3]Associate Professor, Faculty of Civil Engineering., University of Sistan & Baluchestan, Zahedan, Iran, E-mail: mazhdary@eng.usb.ac.ir.

head spillways in upstream than linear spillway that helps the passing of flooding and increases the storage capacity of the reservoir under current conditions (Crookston, 2010). To control the upstream water head and flow capacity, spillway with curvature in plan are almost optimal design. For designers, choosing an optimized design for a particular position can be difficult, because the designing data are limited for much geometric design (Johnson and Savage, 2006).

Since early 1950, the behavior of weir has widely investigated by U.S. Army Corp of Engineers (Bahmani et al., 2010). Bradley (1945) identified four types of flow over dam with ogee profiles. Type. 1 categorized a rapid variable flow of the supercritical over weir; type 2 is a stationary hydraulic jump on weir; Type 3 is a submerged jump and type 4 for weir submergence. Cassidy (1965) obtained discharge coefficient, pressure distribution and water surface profiles for a particular form of spillway. The results of the numerical analysis of flow over spillway were almost identical with the experimental results, and the results of this research indicated a low impact of viscosity at the free surface. Savage & Johnson (2001) developed a study to compare flow parameters in a standard ogee spillway using a physical model, mathematical models and available research records. Finally, a reasonable harmony was observed between the physical and numerical models. Chatila and Tabbara (2004) examined a computational model of the flow over ogee spillway. In this study, regular profiles of the flow over ogee spillway were examined measured the fluid free surface for several levels of flow over weir. Finally, it was shown that the free surfaces of flow predicted by the numerical model were in good agreement with experimental profile of the flow in entire body of weir. Dargahi (2006) conducted an experimental and three-dimensional numerical study of weir with free flow surface. Through their study, the water surface profile and discharge coefficients were predicted based on the water head over the weir with the accuracy of 1.5 to 2.9. Also. Savage & Johnson (2006) studied physical and numerical comparison of flow over ogee spillway in the presence of tail water. The comparison showed that numerical modeling can accurately predict the rate of flow over the spillway and the pressure distribution on the spillway. The results of this study provide users of numerical models performance information that can be used to aid them in determining which tool to use to effectively analyze dams and their associated spillways. Tullis and Neilson (2008) carried out the performance of submerged ogee spillway and proposed a relationship for discharge calculation. The results showed that for submergence levels <0.70, the head-discharge relationship was relatively independent of the tail water elevation, but at higher submergence levels, this was not the case. For submergence values <0.8, the submergence head-discharge data were best predicted using the free-flow head-discharge relationship. For submergence values <0.8, the accuracies of all but one of the head discharge relationships were very poor. For such high submergence levels, more accurate methods are needed for predicting submerged ogee-crest head-discharge relationships. Hunt et al. (2008) evaluated the convergence effects of the lateral walls in stepped spillway. Overall results indicated that flow behavior of the two sides of spillway is the same; transverse waves through the body of spillway were not observed; Furthermore, the water surface profiles showed that flow depth next to wall rapidly increased at the beginning of the convergent part. Khosrojerdi (1997), studied broad crest weirs in direct and curvature illustrations. He suggested that the axial arc, in addition to the structural stability toward the upstream, leads to the increase of discharge coefficient. Also, Khosrojerdi and Mehrjerdi (2007) stimulated the field of passing flow over ogee spillway using fluent software in three-dimensional condition. According to the results, discharge coefficient, static pressure and flow rate within the ogee section is more in the upstream curvature than downstream curvature and direct spillway.

The most investigations performed in this area were about ogee spillway with direct crest and also a few studies have been conducted on spillway with curvature plan and convergent walls. The

present study aims to determine the discharge coefficient over ogee spillway with curvature in plan and convergent walls by using experimental method.

2. Material and method

The experiments were conducted in Soil Conservation Watershed Management Research Institute- Tehran-Iran, using physical model of ogee spillway of Garmi Chay dam in scale 1:50. A reservoir with dimensions 2 m long, 1.80, width, 1.20 m depth were employed. A stilling basin with dimensions of 2 m length, 1.30 m width and 0.6 m height and then the stilling basin of the flume with dimensions 1.5 m long, 0.6 Width, 0.6 m depth were used. The ogee profile of Garmin Chai dam spillway has been designed according to USBR standard. An overview plan and section of the spillway is shown in Figs. 1 and 2. The geometry of spillway model is adjusted using Froude similarities. Spillway is curved and built using CNC milling machine with 0.05 mm precision by Teflon blocks. Lateral walls and downstream channel were built of Plexiglas. The experiments were carried out with eight discharges: 14.14, 16.97, 19.12, 22.62, 25.46, 28.28, 31.11 and 33.94 lit/sec. The water head over the spillway crest was measured about 4 to 5 times of H from the edge of crest-point gauge with 0.1 mm precision inside the reservoir, where the effect of surface water curvature was not significant. To Supply water, a pump capable of pumping up to 46 liters per second was used and to measure the discharge, a sharp triangular weir with apex angle of 90° was employed and water height on triangular weir was measured by point gauges. Figs. 3 and 4 illustrate general view of physical model of spillway with scale 1:50.

To determine the discharge of water passing over the ogee spillway, the Eq. (1) is used as follows (Ghodsian, 1998).

$$Q = \frac{2}{3} C_d \sqrt{2g}\, L H^{\frac{3}{2}} \tag{1}$$

in which Q= spillway discharge; L= spillways crest length; H= head over the spillway crest; g= gravitational acceleration; and C_d= discharge coefficient.

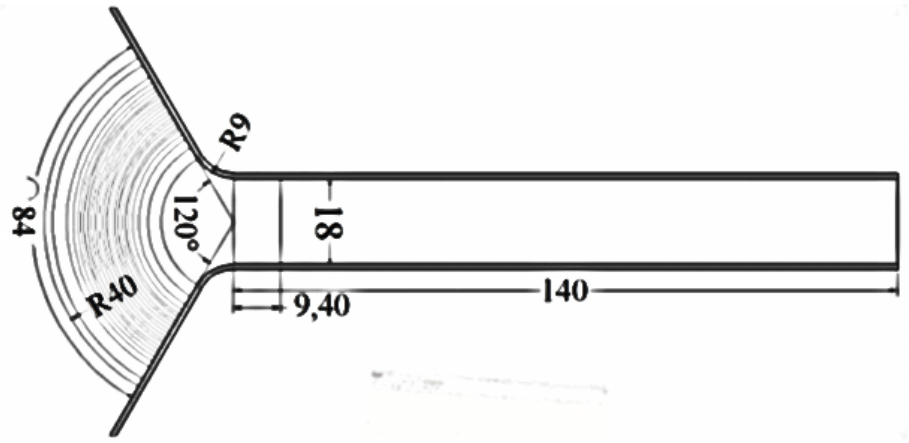


Fig.1 Spillway plan (Dimensions in centimeter)

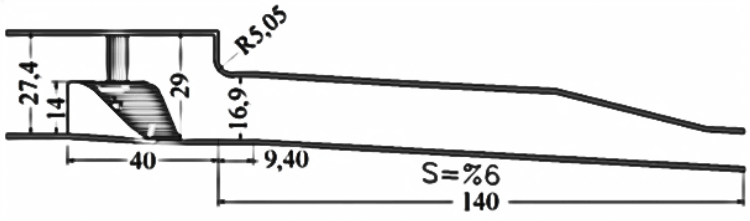


Fig.2 Spillway section (Dimensions in centimeter)

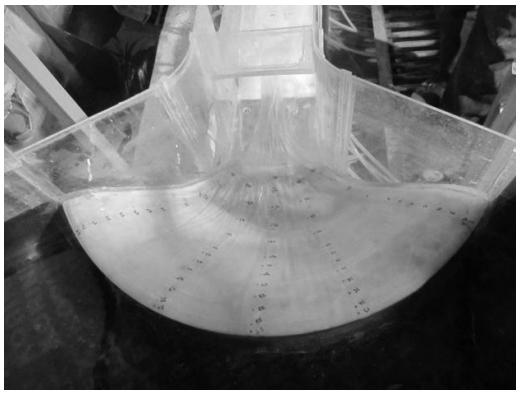


Fig. 3 A view of spillway physical model in scale 1:50

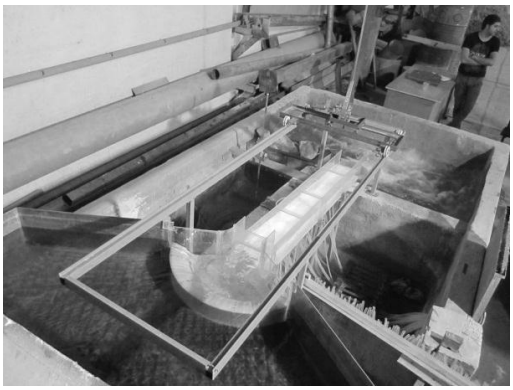


Fig. 4 A view of spillway physical model in scale 1:50

3. Results and Discussions

The relationship between the head over the spillway crest and discharge is shown in Fig.5. With the increase of the discharge, the head over the spillway crest also increases. It is observed that in the discharge range; 14.14 to 25.45 lit/sec, i.e. $0.63<\frac{Q}{Qd}<1.13$, the head over the spillway crest has increasing trend, and the discharge range; 25.45 to 33.94 lit/sec, i.e. $1.13<\frac{Q}{Qd}<1.51$, the head over the spillway crest increase with the more slope in which discharges is greater than 25.45 lit/sec, i.e. $\frac{Q}{Qd}>1.13$, the spillway will be submerged and its efficiency decrease.

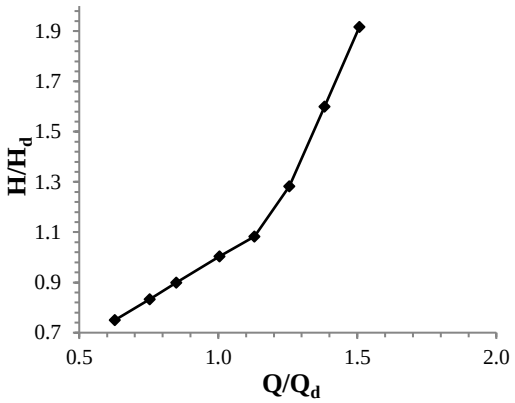


Fig. 5 The variations of head over the spillway crest for different discharge

Fig. 6 indicates that in discharges 0.63<$\frac{Q}{Qd}$<1.13, discharge coefficient has increasing trend which is in $\frac{Q}{Qd} = 1$, $\frac{C}{C_d} = 1$, and the discharge range 1.13<$\frac{Q}{Qd}$<1.51, due to the submerge of spillway, discharge coefficient decrease and the efficiency of spillway also decrease.

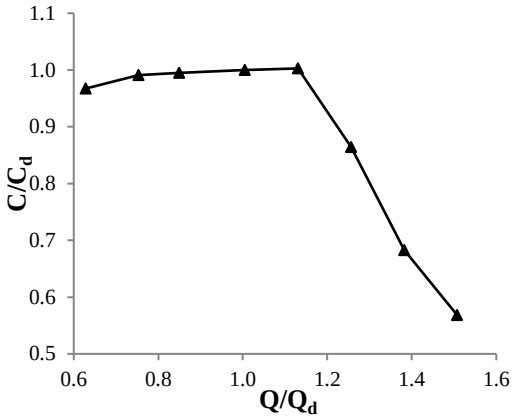


Fig. 6 Discharge coefficients for different discharge

Fig.7 shows the relationship between the head over the spillway crest and discharge coefficient, where physical model with scale 1:50, is compared to USBR standard. In$\frac{H}{H_d} = 1$, $\frac{C}{C_d}$ equals one. In the head range 0.75≤$\frac{H}{H_d}$≤ 1.08, the diagram of head to discharge coefficient has harmony with the diagram of USBR. But in the head range 1.08≤$\frac{H}{H_d}$≤ 1.92, due to the submerged of spillway; it has decreasing trend and the efficiency of weir decreases.

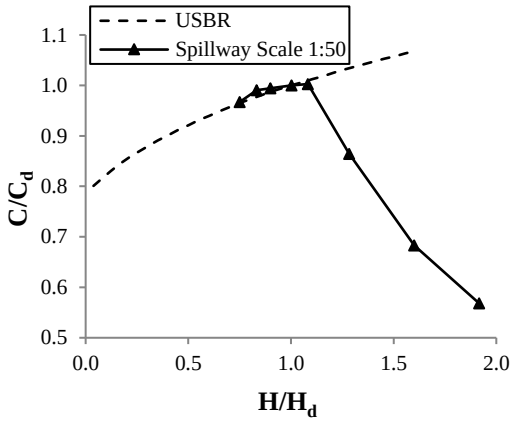


Fig. 7 A comparison of the discharge coefficients for other than the design head

Fig. 8 shows a comparison of the effect of tail water on the discharge coefficient changes in the physical model of spillway with scale 1:50 and USER standard. In this model, the spillway is submerged and its efficiency decreases within$\frac{h_d}{H} < 1$. However, in the diagram of USBR, in $\frac{h_d}{H} <$ 0.7, the spillway is submerged. Discharge coefficient in submerged mode in spillway model with scale 1:50, is smaller than the discharge coefficient of USBR. Since the lateral walls of spillway

are convergent and these convergent walls are connected to a covered downstream channel. As a result this convergence is caused submergence of the spillway in high discharges. The spillway submergence occurs in discharge $\frac{Q}{Qd} > 1.13$, whereas the discharge coefficient decreases in this stage.

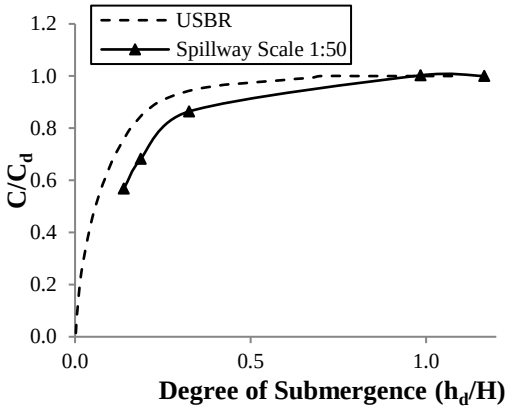


Fig. 8 A comparison of the ratio of discharge coefficients caused by tail water effects

4. Conclusion

This study was determined the discharge coefficient over ogee spillway with curvature in plan and convergent walls by using experimental method of ogee spillway of Garmi Chay dam in scale 1:50. The results showed that in discharges range $0.63 \leq \frac{Q}{Qd} \leq 1.13$, i.e. in the water level $0.75 \leq \frac{H}{H_d} \leq 1.08$, the increase of discharge coefficient and consequently the efficiency of spillway were observed and it has also an acceptable harmony with the diagram of USBR. But in discharges $1.13 \leq \frac{Q}{Qd} \leq 1.51$, i.e. in the water level $1.08 \leq \frac{H}{H_d} \leq 1.92$, due to the spillway submerge, the discharge coefficient ad as a result the efficiency of spillway decrease.

Acknowledgment

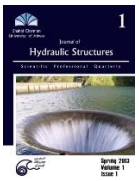
Authors would like to express special appreciation and thanks to technical members of Soil Conservation Watershed Management Research Institute Tehran-Iran, who assisted us in spillway modeling.

References

1. Bahmani, T., Rostami ravari, A., and Tayari, A., (2010), "The determination of discharge coefficient the Roodbal dam spillway by using a physical model", second global conference on integrated water resources management.
2. Bradley, J. N., (1945), "Studies of flow characteristics, discharge and pressures relative to submerged dams", Hydraulic Laboratory Rep, U.S. Dept. of the Interior, Bureau of Reclamation, No. 182, Denver.
3. Cassidy, J. J., (1965), "Irrational flow over spillways of finite height", J Mech Eng Div, ASCE; 91(6):155–173.
4. Chatila, J., Tabbara, M., (2004), "Computational Modeling of Flow over an OgeeSpillway", Computers and Structures 82, p.p.1805–1812.

5. Crookston, B. M., (2010), "Labyrinth Weirs", All Graduate Thesis and Dissertations, Utah State University, paper 802.
6. Dargahi, B., (2006), "Experimental study and 3D numerical simulations for a free-Overflow Spillway", Journal of Hydraulic Engineering, ASCE, Vol. 132, No. 9.
7. Ghodsian, M., (1998), "Viscosity and Surface tension Effects on Rectangular Weir Flow", International Journal of Engineering Science, Iran University of Science & Technology, Vol.9, No.4, pp. 111-117.
8. Hunt, S.L., Kadavy, K.C., Abt S.R, and Temple, D.M., (2008), "Impact of Converging Chute Walls for Roller Compacted Concrete Stepped Spillways", Journal of Hydraulic Engineering, ASCE, Vol. 134, No.7.
9. Johnson, M.C., and Savage, B.M, (2006), "Physical and Numerical Comparison of Flow over Ogee Spillway in the Presence of Tail water", Journal of Hydraulic Engineering, Vol.132, No.12.
10. Khosrojerdi, A., "Study of discharge coefficient with a weir broad crest centered arches using hydraulic model", (1997), M.Sc thesis, Islamic Azad University Branch of Tehran Science and Research.
11. Khosrojerdi, A., Mehrjerdi, M., (2007), "Hydraulic checking ogee spillway in arc axis conditions", 9th Seminar on Irrigation and reduce evaporation.
12. Savage, B. M., and Johnson, C. M., (2001), "Flow over ogee spillway physical and numerical model case study", Journal of Hydraulic Engineering. ASCE, Vol.127, No.8, 640-649.
13. Tullis, B. P., and Neilson, J., (2008), "Performance of Submerged Ogee-Crest Weir Head-Discharge Relationships", journal of Hydraulic Engineering, ASCE, Vol. 134, No. 4.

Journal of Hydraulic Structures
***J. Hydraul. Struct.*, 2016; 2(1):34-47**
DOI: 10.22055/jhs.2016.12649



Shape Optimization of an abrupt contraction using numerical streamlining

Reza Yousefian[1]
Seyed Fazlolah Saghravani[2]

Abstract

This research was conducted to find a reliable technique to shape an abrupt contraction for minimizing the energy loss. The method may find broader applications in design of variety of transitional cross-sections in hydraulic structures. The streamlines in a 2-D contraction were calculated through solving the potential flow equations in rectangular and curvilinear coordinates. The natural cubic spline equations were applied to approximate the shape of streamlines. The streamlines close to the solid boundary, usually those that represent 5 and 95 percent of the discharge, were repeatedly mapped onto the solid boundary in a trial and error procedure until a negligible difference between two consecutive shapes was achieved. This procedure was applied through a code developed in C++, namely Streamlining Program Code or SPC. The initial and final shapes were used to validate SPC by the help of a robust CFD software, OpenFOAM. In a 2-D contraction with contraction ratio of 5, entrance velocity of 1 m/s and outlet pressure of atmosphere (P = 0 pa), the maximum spatial difference between the stream lines found by the code and OpenFOAM was limited to 2.74% that occurred in the entrance of the contraction. Finally, according to the validation, the streamlining technique and the code could successfully applied to shape optimization of hydraulic structures.

Keywords: hydraulic design; numerical technique; streamlining; grid generator; verification; OpenFOAM.

Received: 14 January 2016; Accepted: 27 June 2016

1. Introduction

In the recent decades, with the advancement of computational technology, the use of robust numerical methods to solve the complex equations of fluid mechanics became more feasible. The streamlined based design is a design philosophy to form the solid bodies so that offers the

[1] Department of Civil Engineering, Shahrood University of Technology, Shahrood, Iran, saghravani@shahroodut.ac.ir, Tel.: +98-23-32300259; fax: +98-23-32300259. (**Corresponding author**)
[2]Department of Civil Engineering, Shahrood University of Technology, Shahrood, Iran

least resistance to fluid flow. Since the available new literature on details of streamlining techniques is limited, more research in this area seems to be useful.

The area of streamlined design has received great attention within different fields of application. Prior to 1960s, axial compressor and turbine design were based on streamlining, relied considerably on correlations of experimental data. Analytical research began to have greater impacts on this largely practical design approach towards the end of the 1950s. Since early 1960s, modern turbo-machinery design has mostly relied on CFD to develop three-dimensional blade sections. Nowadays, simple methods accompanied by empirical input are used for the mean-line design and flow modelling. These calculations are often left to the experienced designers who utilize CFD tools to reach to a good design [1]. In 2003, research on stationary fluid-structure interaction (FSI) problems was implemented for the sake of analysis and shape optimization of strongly coupled FSI systems by general, efficient and gradient based methods [2]. An optimized design for streamlining an intake of a small-scale turbojet engine carried out by Amirante et al. in 2007 [3]. In 2009, the streamlining procedure was used to design an inlet guide vane system of a mini hydraulic bulb-turbine, 3-stage axial-flow compressor and axial-flow hydraulic turbine [4] [5] [6]. Similarly, streamlining was applied to design and develop clamping and mold ejection systems to use in gravity die-casting machine and in optimization of bridge piers cross-section [7] [8].

This paper presents a numerical technique for streamlining of transitional cross-sections in hydraulic structures that carry incompressible-irrotational flow. This method is capable of streamlining cross-sections with positional constraints as well as considering the upstream characteristics in streamlining procedure. Note that, as streamlining leads transitional flows to be irrotational, assumption of irrotationality does not limit the applications of this streamlining technique. In this approach, first, the potential flow equations could be solved by any desired numerical method to obtain the streamlines, which the finite difference method (FDM) was used here for the sake of simplicity and attracting to a broad range of readers. Then, a streamline would be selected and mapped on the solid boundary to form a new curved boundary. Thereafter, accompanied by generating structured grids, the problem would be solved through iterative scheme for calculating the new streamlines. This iterative procedure continues until the differences between the coordinates of previous and current solid boundaries become less than the allowed tolerance. Eventually, a problem was adapted and solved to verify the applied technique by modelling obtained geometries in OpenFOAM.

2. Governing equations

This technique aimed to shape the cross-sections in reference to the streamlines coordinates, and thus, it needs to solve a stream function that is the description of the flow. The stream function satisfies the law of conservation of mass for incompressible, two-dimensional flows. According to the mass conservation law, the continuity equation can be written as equation **Error! Reference source not found.**.

$$-\frac{1}{\rho}\frac{D\rho}{Dt}=\frac{\partial u_i}{\partial x_i} \tag{1}$$

The density of fluid does not change appreciably along the fluid path under certain conditions according to the Boussinesq approximation. The conditions hold in most liquid flows and in the flows of gases where the speeds are less than about 100 m/s [9].

For any flow, a function $\psi(x,y,t)$ is defined as stream function that satisfies the continuity

equation. In the case of irrotational flow, by substituting the definitions of stream function into the equation of vorticity, the so called Laplas Equation of stream function, the main differential equation for streamlining techniques, would be derived as Equation (2) [10].

$$\nabla^2\psi = \frac{\partial^2\psi}{\partial x^2} + \frac{\partial^2\psi}{\partial y^2} = 0 \tag{2}$$

3. Solving governing partial differential equation (PDE)

In order to solve the governing PDE, FDM was selected as approximations convert the partial derivatives to finite difference expression. As equation **Error! Reference source not found.** is an elliptic equation, point successive over-relaxation method (PSOR) was chosen for solution algorithm. In this algorithm, finite difference equations are solved at grid points. Therefore, first, grid points within the domain as well as the boundaries coordinates must be specified and then solving the PDE as algebraic equation is accomplished by finite difference formulations.

As the domains are categorized into two grid systems, structured and unstructured grids, the grid system of this technique was considered as structured with rectangular and nonrectangular physical domains [10].

3.1. Solving governing PDE within rectangular domain.

In the first stage, the domain is assumed as rectangular and grid points are specified as coincident with the boundaries of physical domain, thus the grid generation will be considerably simple. Therefore, the initial streamlines are obtained by utilizing PSOR method for solving the stream function equation. In this method, a second-order central differencing is used for the representation of the PDE. Thus, model Equation **Error! Reference source not found.** is approximated as follows.

$$\psi_{i,j}^{k+1} = (1-\omega)\psi_{i,j}^{k} + \frac{\omega}{2(1+\beta^2)}\left[\psi_{i+1,j}^{k} + \psi_{i-1,j}^{k+1} + \beta^2\left(\psi_{i,j+1}^{k} + \psi_{i,j-1}^{k+1}\right)\right] \tag{3}$$

In this equation, β is the ratio of step-sizes defined as $\beta = \Delta x/\Delta y$. The variable ψ is solved at each grid point by using initial guessed values or previously computed values. Thus, k is defined as iteration level and since PSOR uses a trend to accelerate the solution procedure, the relaxation parameter ω which is necessary to be $0 < \omega < 2$ utilized in equation **Error! Reference source not found.** [10]. Thereafter, one of the streamlines in the rectangular domain is picked to map on the solid boundaries for creating the problem with new boundaries that will be solved in the next stage.

3.2. Solving governing PDE within nonrectangular domain

To solve the new domain with curved streamlined boundaries, a transformation form of physical space to computational space should be employed. This transformation specifies a generalized coordinate system that converts the nonrectangular physical space into the rectangular, constant step-size, computational space. A body fitted coordinate system would be selected as the generalized coordinate system, where two coordinate axis ξ and ζ are on the surface along the stream-wise and circumferential directions, and the third coordinates η is

normal to the surface. Therefore, for transforming the physical space, first transformation of the governing PDE equation is accomplished, and then the grid would be generated by partial differential methods [10].

3.2.1. Transformation of the governing PDE

By defining the following relations between the physical and computational spaces, the chain rule is used for transforming the partial differentiation expressions.

$$\xi \equiv \xi(x,y), \eta \equiv \eta(x,y) \tag{4}$$

$$\frac{\partial}{\partial x} = \frac{\partial \xi}{\partial x}\frac{\partial}{\partial \xi} + \frac{\partial \eta}{\partial x}\frac{\partial}{\partial \eta}, \frac{\partial}{\partial y} = \frac{\partial \xi}{\partial y}\frac{\partial}{\partial \xi} + \frac{\partial \eta}{\partial y}\frac{\partial}{\partial \eta} \tag{5}$$

Therefore, the model PDE (equation **Error! Reference source not found.**) would be transformed from physical space to computational space by applying equations **Error! Reference source not found.** as follows [11].

$$\frac{\partial^2 \psi}{\partial \xi^2}\left[\left(\frac{\partial \xi}{\partial x}\right)^2 + \left(\frac{\partial \xi}{\partial y}\right)^2\right] + \frac{\partial^2 \psi}{\partial \eta^2}\left[\left(\frac{\partial \eta}{\partial x}\right)^2 + \left(\frac{\partial \eta}{\partial y}\right)^2\right] + 2\frac{\partial^2 \psi}{\partial \xi \partial \eta}\left[\left(\frac{\partial \eta}{\partial x}\right)\left(\frac{\partial \xi}{\partial x}\right) + \left(\frac{\partial \eta}{\partial y}\right)\left(\frac{\partial \xi}{\partial y}\right)\right] + \frac{\partial \psi}{\partial \xi}\left(\frac{\partial^2 \xi}{\partial x^2} + \frac{\partial^2 \xi}{\partial y^2}\right) + \frac{\partial \psi}{\partial \eta}\left(\frac{\partial^2 \eta}{\partial x^2} + \frac{\partial^2 \eta}{\partial y^2}\right) = 0 \tag{1}$$

The transformed equation would be solved in the computational domain. In addition, it should be mentioned that the transformation derivatives (metrics) should be known in advance by using a numerical method to solve the metrics in the computational space. Generally, to solve the metrics with less complexity, Jacobian of transformation, J, is defined to formulate the metrics [10].

$$J = \frac{1}{\left(\frac{\partial x}{\partial \xi}\frac{\partial y}{\partial \eta} - \frac{\partial y}{\partial \xi}\frac{\partial x}{\partial \eta}\right)} \tag{2}$$

$$\frac{\partial \xi}{\partial x} = J\frac{\partial y}{\partial \eta}, \frac{\partial \xi}{\partial y} = -J\frac{\partial x}{\partial \eta}, \frac{\partial \eta}{\partial x} = -J\frac{\partial y}{\partial \xi}, \frac{\partial \eta}{\partial y} = J\frac{\partial x}{\partial \xi} \tag{3}$$

3.2.2. Grid generation

In this streamlining technique, the elliptic grid generators that work well in the domain with specified physical boundaries, were used as grid generator. For generating the grid with curved boundaries, the x and y coordinates of solid boundaries should be defined and thereafter a system of elliptic PDEs with the form of equations (4) is solved to determine the x and y coordinates of computational domain grid points in the physical space.

$$\frac{\partial^2 \xi}{\partial x^2} + \frac{\partial^2 \xi}{\partial y^2} = 0, \frac{\partial^2 \eta}{\partial x^2} + \frac{\partial^2 \eta}{\partial y^2} = 0 \tag{4}$$

Equation (4) would be solved by PSOR iterative technique mentioned in section 0. Because of computation of these PDEs takes place in computational rectangular domain with uniform grid spacing, the interchanging of the dependent variables (x, y) and independent variables (ξ, η) are required. For this purpose, the mathematical expressions should be employed to transform the elliptic PDEs to equations (5).

$$a\frac{\partial^2 x}{\partial \xi^2} - 2b\frac{\partial^2 x}{\partial \xi \partial \eta} + c\frac{\partial^2 x}{\partial \eta^2} = 0, a\frac{\partial^2 y}{\partial \xi^2} - 2b\frac{\partial^2 y}{\partial \xi \partial \eta} + c\frac{\partial^2 y}{\partial \eta^2} = 0 \tag{5}$$

$$a = \left(\frac{\partial x}{\partial \eta}\right)^2 + \left(\frac{\partial y}{\partial \eta}\right)^2, b = \left(\frac{\partial x}{\partial \xi}\right)\left(\frac{\partial x}{\partial \eta}\right) + \left(\frac{\partial y}{\partial \xi}\right)\left(\frac{\partial y}{\partial \eta}\right), c = \left(\frac{\partial x}{\partial \xi}\right)^2 + \left(\frac{\partial y}{\partial \xi}\right)^2 \tag{6}$$

After all, coordinates of the grid points in physical space (x, y) would be specified for the purpose of determining the metrics and ψ values in order to solve the governing PDE in nonrectangular domain [10].

4. Verification of the streamlining technique

In order to verify the proposed streamlining technique, a 2D contraction problem for the sake of streamlining the entrance cross-section was chosen. The specifications of the problem was illustrated in Figure 1. In this problem, there were two pairs of positional constraints showed by cross markers in the entrance section to carry out streamlining in the boundaries between each pair of constraints. The fluid was assumed as water and the characteristics of boundaries and flow are as follows.

Inlet velocity in x-direction	1 m/s
Inlet velocity in y-direction	0 m/s
Outlet pressure	0 Pa
Density of water	1000 kg/m^3
Kinematic viscosity	1.0E - 6 m^2/s

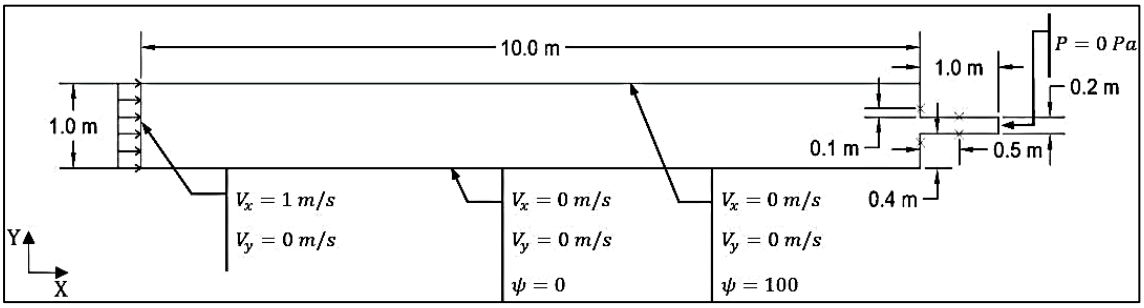


Figure 1. Dimensions and boundary conditions of the problem

A streamlining programing code (SPC) based on details discussed in section 0, was written in C++ programming language by using the Microsoft Visual Studio Express edition 2013 as compiler. In this software, the standard libraries of C++ were used for calculations and the Fast Light Tool Kit 1.3.3 (FLTK) was utilized as Graphical User Interface (GUI) for illustrating the streamlines and streamlined cross-sections. Also, Open Source Field Operation and Manipulation (OpenFOAM) software with C++ library was employed to verify SPC. The version 2.2.2 of OpenFOAM was executed on Ubuntu12.04. In this application, the grid generated by blockMesh, potentialFoam used as solver and the version 3.12.0 of paraView utilized for post-processing.

5. Results and discussions

The problem was solved by SPC and OpenFOAM software; by comparing the results of SPC and OpenFOAM software, the correctness of this numerical technique would be investigated in the following.

5.1. Results and solution algorithm of SPC

In order to streamline the contraction problem stated above, first the problem was solved in the rectangular domain, shown in Figure 1, by scheme discussed in section 0. The boundary conditions applied for this problem in SPC were shown in Figure 2. It should be noted that the boundary conditions of the stream function values in inlet and outlet were calculated based on mass conservation law. In this figure, is the node number in inlet and outlet sections.

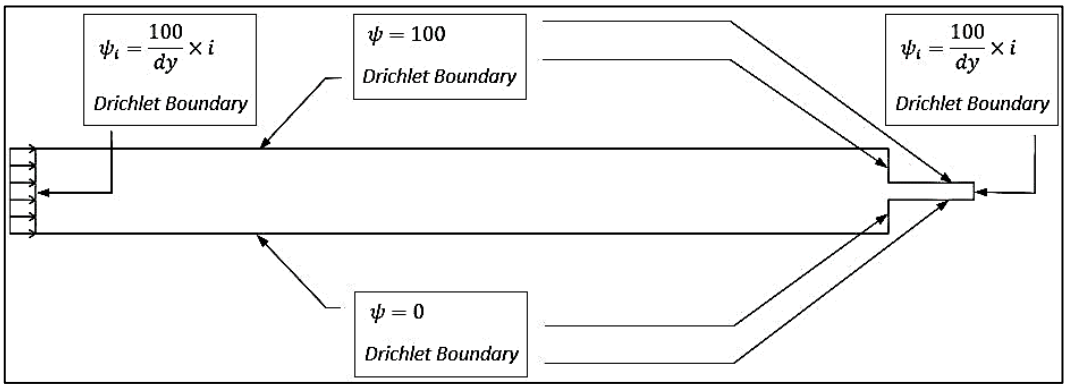


Figure 2. Boundary conditions of models in SPC

The grid generated for the rectangular space had constant step-size in x and y direction and also the value of step-size was selected as 0.05 m and equaled to each other in both directions. Streamlines of this problem were obtained as a result of the first loop of streamlining, Figure 3.

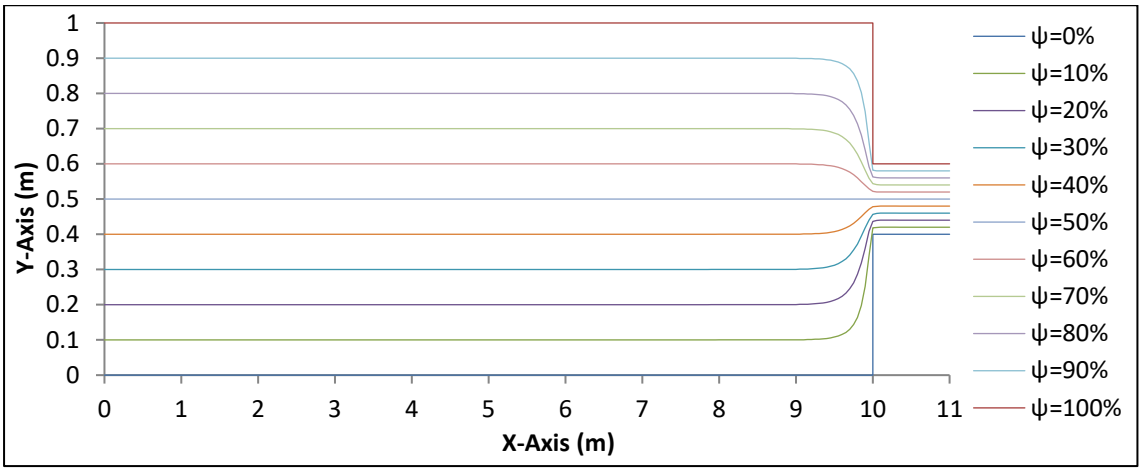


Figure 3. Streamlines obtained in the first loop of streamlining in SPC

After obtaining streamlines in the rectangular domain, the streamline of $\psi = 95\%$ shown by blue line in Figure 4 selected to map on the solid boundary. For this purpose, by moving the selected streamline to the constraints mentioned in the problem, the new solid boundary, illustrated by red line in Figure 4, was formed.

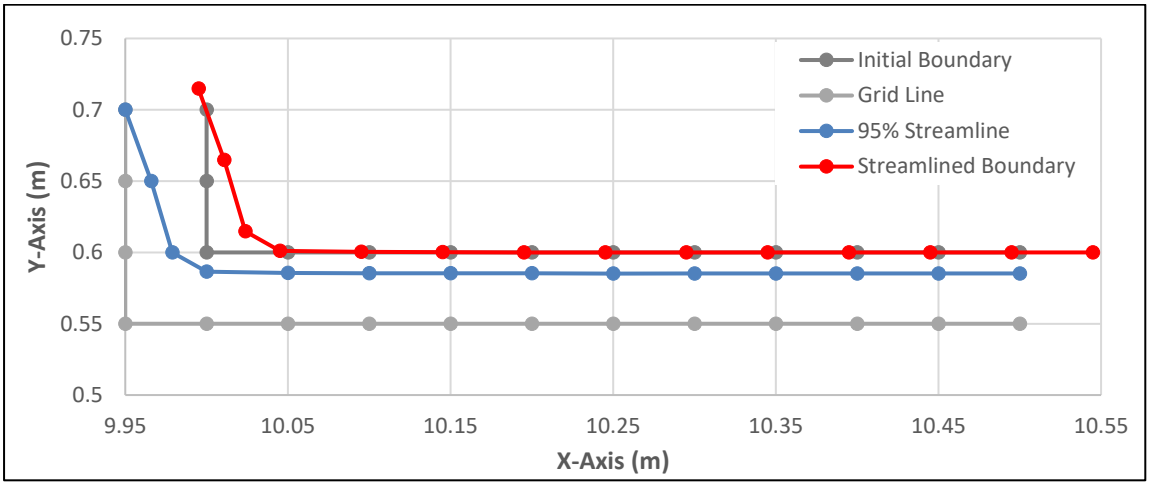


Figure 4. Mapping a streamline on solid boundary

Therefore, the new problem with curved boundaries would be generated. This problem with nonrectangular domain was solved by the technique explained in section 0. Figure 5 illustrates the grid generated by SPC for this problem.

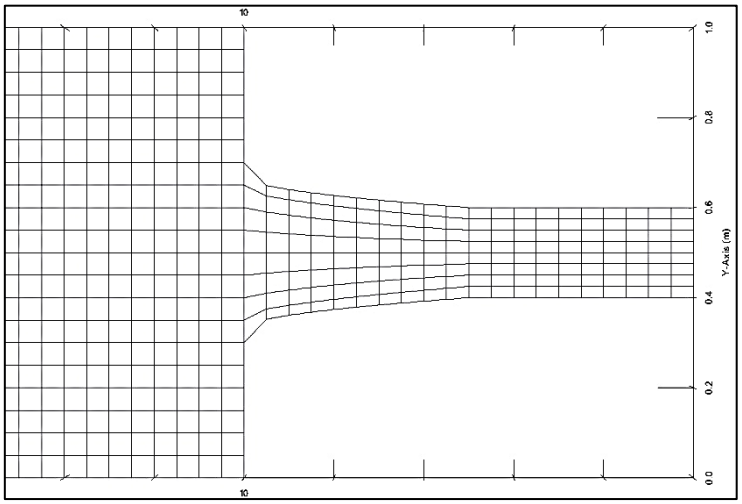


Figure 5. Grid generated by SPC

Finally, by defining the convergence criteria as the positional difference between selected streamline, here 95% streamline, and the previous streamlined boundary, this iterative procedure was carried out until the differences became less than 1.0E-11 m and then the streamlined section was obtained. Figure 6 illustrates the streamlined cross-section and streamlines calculated in this domain that as the grid points in the target area increased, the shape would be smoother.

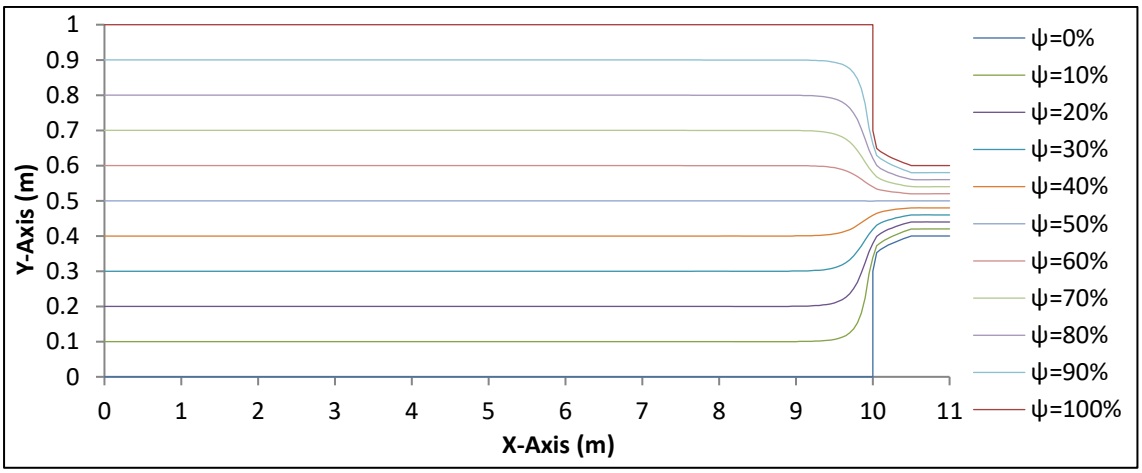


Figure 6. Streamlined cross-section and streamlines in curved boundary domain obtained from SPC

5.2. OpenFOAM properties and results

For modelling the problem to verify SPC, two problems with rectangular and nonrectangular spaces, illustrated in Figure 3 and Figure 6, were modelled in OpenFOAM. Velocities and pressures conditions of boundaries assigned to the models are shown on Figure 7. Noted that the boundary conditions of both models were the same.

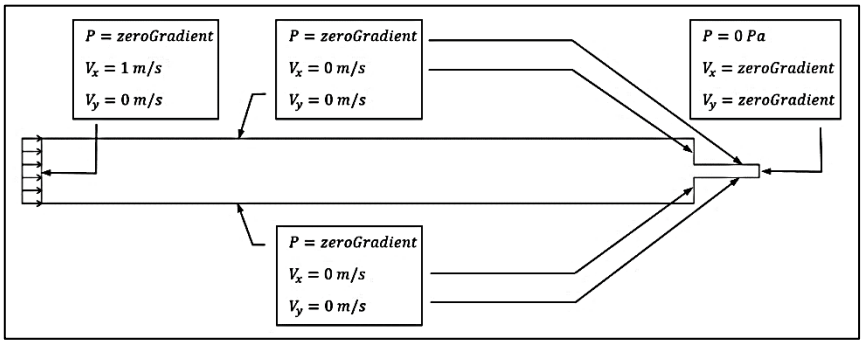


Figure 7. Boundary conditions of models in OpenFOAM

By modelling the problem in OpenFOAM software, grid and stream function accuracy of SPC results were considered as criteria to verify the CFD code. Since there were two models discussed above with rectangular and nonrectangular domain, the cited criteria was studied in these two models. For illustration purposes, Figure 8 and Figure 10 show the streamlines obtained by OpenFOAM and Figure 9 illustrates the grid generated by blockMesh in OpenFOAM. Also these figures would be compared to Figure 3 , Figure 6 and Figure 5, the results of SPC, respectively.

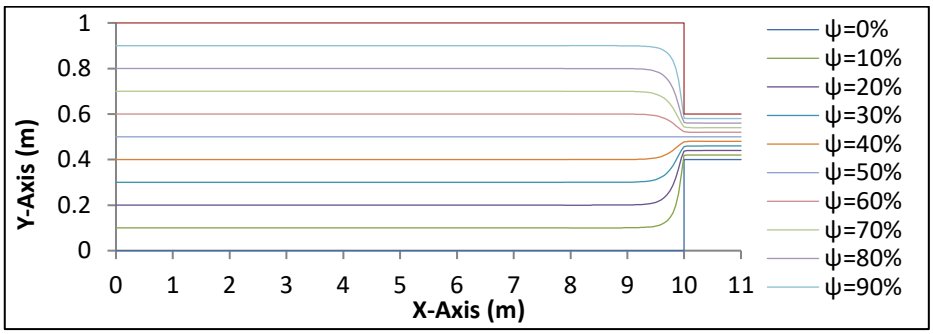


Figure 8. Streamlines of initial model obtained by OpenFOAM

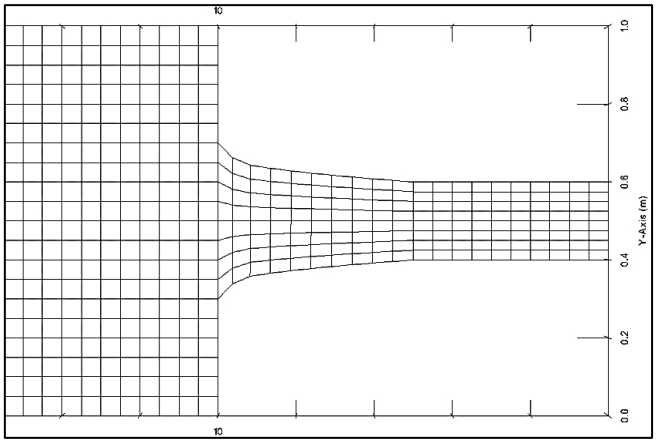


Figure 9. Grid generated by blockMesh in OpenFOAM

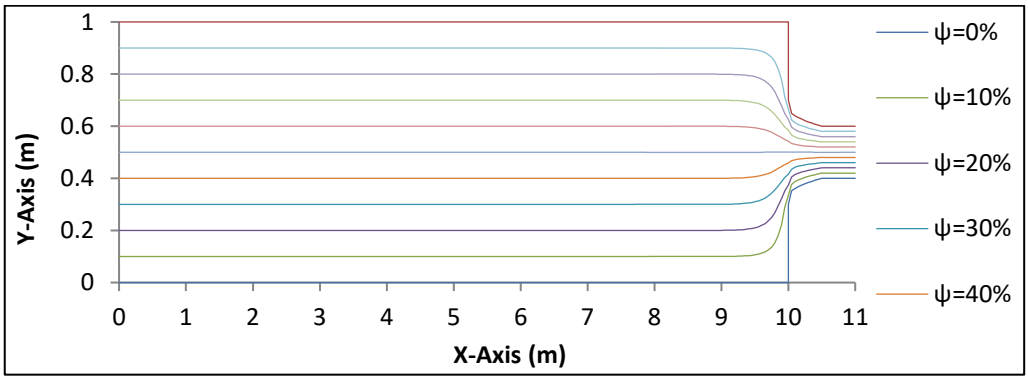


Figure 10. Streamlines of streamlined model obtained by OpenFOAM

5.3. Results comparison

The nodes coordinates of OpenFOAM and SPC models were compared to each other in the following to verify the grids. In rectangular domain, the grids were the same as expected but some differences in grid points coordinates of nonrectangular domain were observed. The maximum positional difference of grid points generated by blockMesh in OpenFOAM and SPC was 0.018 m in x-direction. Figure 11 illustrates the position of maximum differences in the domain.

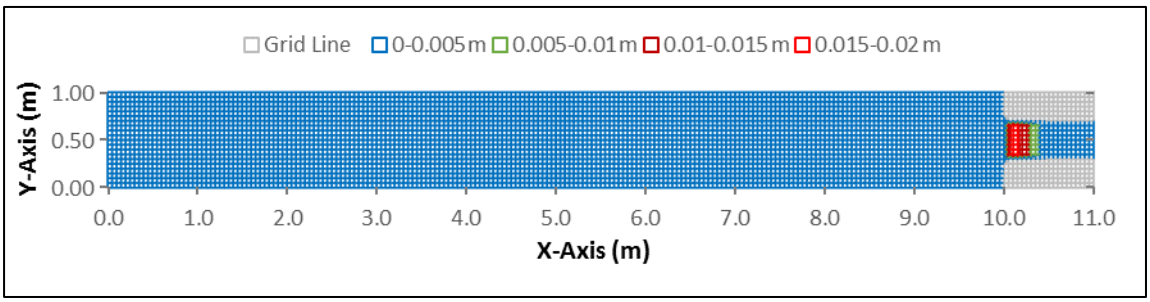


Figure 11. Position of maximum differences between x-coordinate of grids

The differences in y-direction are as shown in Figure 12. The maximum difference between corresponding nodes was 0.014 m.

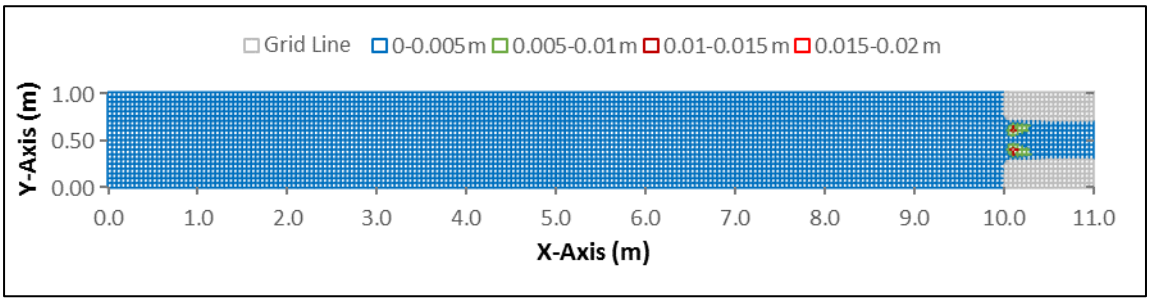


Figure 12. Position of maximum differences between y-coordinate of grids

Since the differences in the domain were in a small part of the domain, Figure 13 and Figure 14 were prepared to show more precise place of differences.

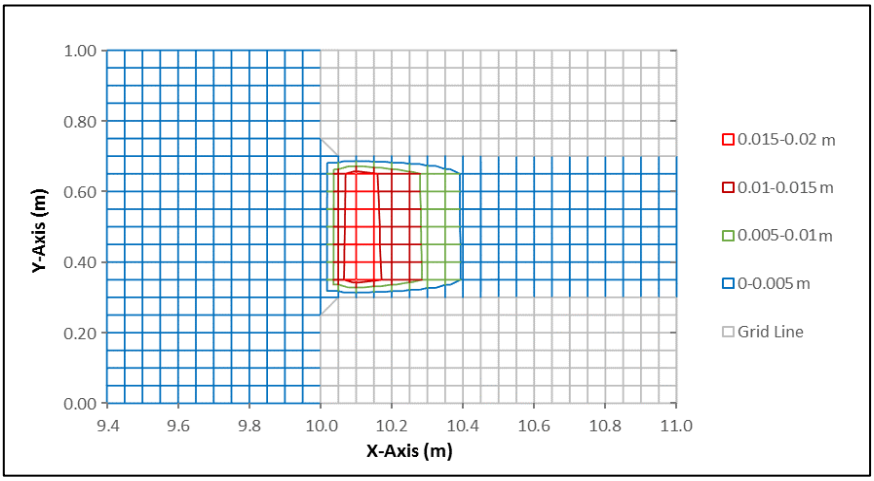


Figure 13. Magnified position of maximum differences between x-coordinate of grids

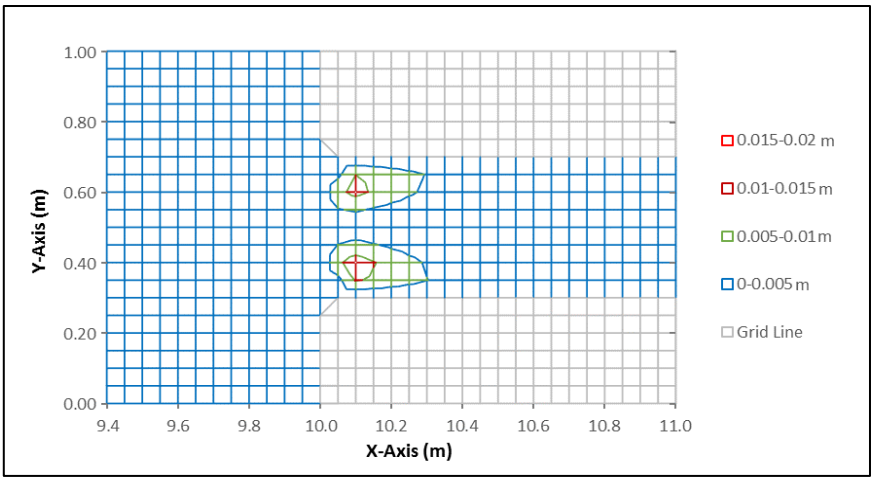


Figure 14. Magnified position of maximum differences between y-coordinate of grids

Although differences existed in grids generated by OpenFOAM and SPC were less than 5% but unchanging x-coordinate of grids in SPC, differences in approximation methods and schemes employed in these models are accounted for these displacements.

For considering the values of stream function in both models by OpenFOAM, the non-dimensional stream function values of grid points in physical domain (with the same coordinates) were calculated and compared to each other. As shown in Figure 8, the maximum difference between stream function values in rectangular domain models was 1.3E -4%. Since the grids of both OpenFOAM and SPC were the same, the value was expected.

In nonrectangular models, the maximum difference between each node of the same coordinates was 2.740%, Figure 15.

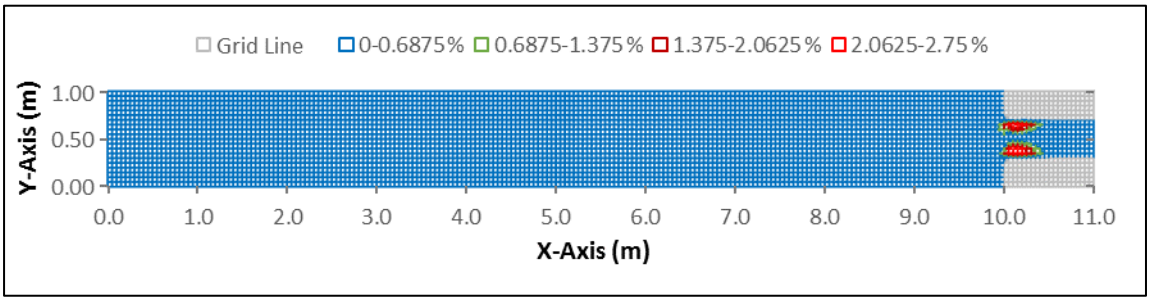


Figure 15. Position of maximum differences between ψ values

Figure 16 illustrates more details of differences showed in Figure 15 to compare the stream function results.

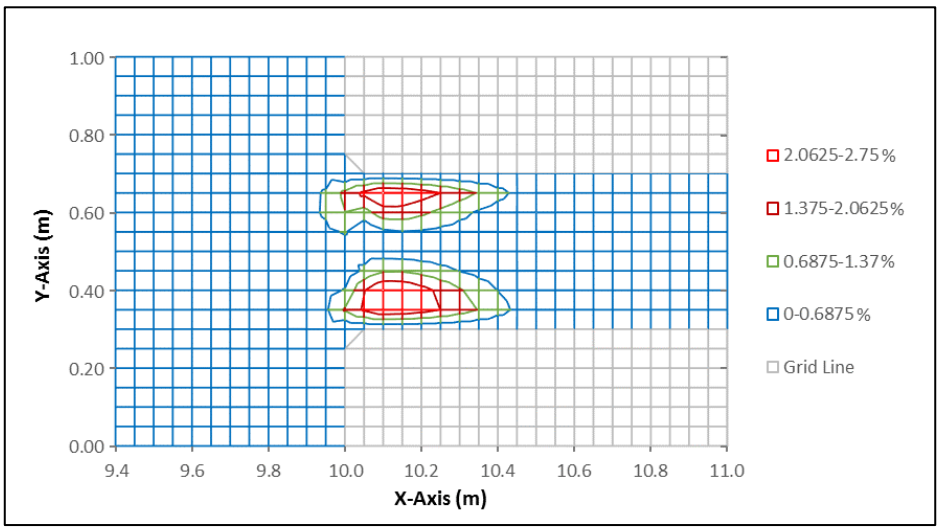


Figure 16. Magnified position of maximum differences between ψ values

The following issues could cause some inconsistencies observed in the stream function values. As OpenFOAM solves the PDEs by finite volume method (FVM), approximations used in this application differ from SPC, which utilizes FDM. In addition, solution schemes and numerical technique employed by these CFD tools make some differences in results of modelling. Moreover, by considering the positions of differences in grids of models, Figure 13 and Figure 14, and position of maximum differences of stream function values shown in Figure 16, the differences in stream function values would be expected. Therefore, according to these reasons include differences in grid points coordinates and also the methods employed for modelling in these CFD tools, the maximum difference of stream function value was accepted as allowable value for verification.

6. Conclusions

A transitional cross-section with two positional constraints in a contraction problem was designed and streamlined by the proposed numerical technique that is able to consider the effects

of upstream flow and positional constraints on the shape of cross-sections in order to study the numerical aspects of streamlining in this application field. For this purpose, the grid generation technique, methods of solving rectangular and nonrectangular domains for streamlining in SPC were investigated with the help of OpenFOAM software. Comparison of stream function values and those from the modelling of both types of domains in OpenFOAM illustrated that the grid generation technique plays an important role in accuracy and correctness of numerical results. In the case of rectangular domain, FVM and FDM provide almost identical answer to the problem, while for nonrectangular domain some differences are observed. The results of comparing the nonrectangular grids demonstrated that although a problem can be solved within a one directional grid, for the sake of accuracy, the grid should be generated in all directions of the problem. Furthermore, as many problems in numerical methods are divided to some blocks that are rectangular or nonrectangular, for grid generation procedure, all blocks of the problem should be considered as a unit block until the sudden change in the grid does not affect the results. Finally, modelling grids and both types of domain in OpenFOAM showed that in general, there was a good agreement between the results of SPC and OpenFOAM. Therefore, the numerical technique employed in SPC to streamline different transitional sections is verified and capable to improve the other streamlining techniques.

7. Acknowledgements

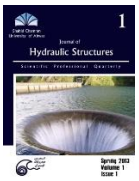
The authors would like to thank Dr. A. A. Pouyan and Ms. Z. Elmi for their assistance in the course of this research.

References

1. J. H. Herlock and J. D. Denton, "A review of some early design practice using computational fluid dynamics and a current perspective," *Journal of Turbomachinery*, vol. 127, pp. 5-13, January 2005.
2. E. Lund, H. Moller and L. A. Jakobsen, "Shape design optimization of stationary fluid-structure interaction problems with larg displacements and turbulence," *Structural and Multidisciplinary Optimization*, vol. 25, pp. 283-392, 2003.
3. R. Amirante, L. A. Catalano, A. Dadone and V. S. E. Daloiso, "Design optimization of the intake of a small-scale turbojet engine," *Computer Modeling in Engineering and Sciences*, vol. 18, pp. 17-30, 2007.
4. L. M. Ferro, L. M. Gato and A. F. Falcao, "Design and experimental validation of the inlet guide vane system of a mini hydraulic bulb-turbine," *Renewable Energy*, vol. 35, pp. 1920-1928, 2009.
5. J. Takachi Tomita and J. R. Barbosa, "The use and comparison of avialabe design tools for a 3-stage axial-flow compressor: meanline, streamline curvature and cfd," in *20th International congress of mechanical engineering*, Gramado, 2009.
6. V. Prasad, V. K. Gahlot and P. Krishnamachar, "CFD approach for design optimization and validation for axial flow hydraulic turbine," *Indian Journal of Engineering and Material Sciences*, vol. 16, pp. 229-236, August 2009.

7. V. Sharma and O. PrakashShukla, "Design and development of clamping and ejection systems for mould used on gravity die casting machine," *International Journal of Engineering and Technology*, vol. 2, no. 10, pp. 890-897, 2013.
8. L. Junhong and T. Junliang, "Streamlining of bridge piers as scour countermeasures: optimization of cross section," in *Transport Research Board 94th Annual Meeting*, Washington, 2015.
9. K. P. Kundu and I. M. Cohen, Fluid mechanics, 4th ed., Burlington, Massachusetts: Academic Press, 2010.
10. K. K. Hoffmann and S. T. Chiang, Computaional fluid dynamics, 4th ed., vol. 1, Wichita, Kansas: Engineering Education System, 2000.
11. J. d. Anderson, Computational fluid dynamics; the basics with applications, 1st ed., New York: McGraw-Hill Education, 1995.

Journal of Hydraulic Structures
***J. Hydraul. Struct.*, 2016; 2(1):48-57**
DOI: 10.22055/jhs.2016.12650



Slope Stability Analysis Using a Self-Adaptive Genetic Algorithm

Amir H. Ayati[1]
Hossein M.V. Samani [2]
Ali Haghighi [3]

Abstract

This paper introduces a methodology for soil slope stability analysis based on optimization, limit equilibrium principles and method of slices. In this study, the slope stability analysis problem is transformed into a constrained nonlinear optimization problem. To solve that, a Self-Adaptive Genetic Algorithm (GA) is utilized. In this study, the slope stability safety factors are the objective functions, slip surface parameters are the decision variables and, the equilibrium equations are the problem constraints. The proposed model satisfies all conditions of the equilibrium completely. It is also applicable to problems with different soil layers, variable soil properties and including pore water pressure. The model is applied against a benchmark example and the results are compared with previous studies. Accordingly, it is found computationally efficient and reliable.

Keywords: Slope stability analysis, self-adaptive GA, Method of slices, Equilibrium analysis, Safety factor

Received: 13 January 2016; Accepted: 18 July 2016

1. Introduction

Slope stability analysis is of geotechnical engineering problems that has received considerable attention from researchers worldwide. Equilibrium analyses of slope stability are widely used in design of excavation and embankment slopes. There exist a lot of successful applications and experiences on the limit equilibrium methods which make it very popular

[1] Civil Engineering Department, Faculty of Engineering, Shahid Chamran University of Ahvaz, Ahvaz, Iran, Email: saha.science@gmail.com (**Corresponding author**)
[2]Civil Engineering Department, Faculty of Engineering, Shahid Chamran University of Ahvaz, Ahvaz, Iran
[3]Civil Engineering Department, Faculty of Engineering, Shahid Chamran University of Ahvaz, Ahvaz, Iran

through their simplicity to implement and accuracy of results as well. Indeed, the limit equilibrium methods have been the most widely used methods for slope stability analysis [1]. These methods, in general, satisfy the force and moment equilibrium; boundary conditions and the failure criterion along the slip surface. In context of the limit equilibrium methods, methods of slices are extensively used to cope with complex slope geometries, variable soil properties and the existence of pore water pressure.

Reviewing the literature, the slope stability methods can be categorized in two major groups consisting of the numerical methods, mostly the finite element method [2-4] and analytical methods, mostly based on the methods of slices. The latter encompasses; the ordinary method (1936) [5], simplified Bishop method (1955) [6], simplified Janbu method (1956) [7], Corps of Engineers method (1967) [8], Spencer method (1967) [9], Morgenstern-Price method (1965) [10], Samani and Meidani (2003) [11]. These methods are somehow different in defining the safety factor equations. They also use different assumptions to derive the governing equations and carrying out the stability analyzes as summarized in Table 1.

There are two kinds of solutions for the problem. The first is a simplified solution where the

Table 1. Different methods of slices for slope stability analysis

Method	Assumptions	Equations used	Slip surface
Ordinary method of slices (1936)	• Resultant of side forces (Ei) is parallel to the base of the slice	• Overall moment	Circular
Bishop (1955)	• Resultant of side forces is horizontal	• Overall moment • Vertical forces	Circular
Janbu(1956)	• Location of side force resultants on the sides of the slice (location can be varied) • Uses a correction factor f_o To account for the effect of the inter-slice shear forces.	• Overall moment • Vertical forces • Horizontal forces • Slice moment	Any
Morgenstern and price(1965)	• Inter-slice forces (Xi) related by • V = λ f (x) E form of f (x)	• Overall moment • Vertical forces • Horizontal forces • Slice moment	Any
Spencer(1967)	• Inter-slice forces are parallel	• Overall moment • Vertical forces • Horizontal forces • Slice moment	Any
Samani and Meidani(2003)	• No Assumption	• Overall moment • Vertical forces • Equilibrium of forces in tangential direction to the base of slices	Circular

conditions of static equilibrium are not rigorously satisfied. In this solution, some assumptions are made to obtain the solution in a simple form. The second is a rigorous solution where the equilibrium conditions are completely satisfied [12].

In general, the main features of limit equilibrium methods can be summarized as the following [13]:

1) The sliding body above an assumed slip surface is divided into a number of vertical (or inclined) slices.

2) The strength of the slip surface is mobilized by the same factor of safety, where the cohesion component and the friction component of the strength are reduced equally.

3) Assumptions regarding inter-slice forces are employed to render the problem determinate.

4) The factor of safety is derived from the force or/and moment equilibrium equations.

Table 2. Summary of equations and unknowns associated with limit equilibrium methods

Number of equations	Type of equations
N	Horizontal force equilibrium
N	Vertical force equilibrium
N	Moment equilibrium
N	Mohr-Coulomb failure criterion at the base of slice
$4N$	Total number of equations
Number of unknowns	**Type of unknowns**
N	Total normal force at the base of slice, P_iShear force at the base of slice, S_i
N	Inter-slice total normal force, E_i
$N-1$	Inter-slice shear force, X_i
$N-1$	Point of application of the Inter-slice total normal force
$N-1$	Point of application of the total normal force at the base of a slice
N	Factor of safety
1	Total number of unknowns
$6N-2$	

Note: N is the number of slices, P_i, S_i, E_i, X_i are introduced in figure 2.

The number of equations and unknowns associated with the limit equilibrium methods are presented in Table 2. It shows that the number of available equilibrium equations is less than the number of unknowns in slope stability problems. As a result, the problem is inherently indeterminate. An indeterminate system of equations has an infinite number of solutions. Using engineering judgment and experiences, one may confine the unknown values between a lower and upper limit in order to manage possible solutions. In this context, the problem could be more systematically treated using the optimization techniques. On this basis, the present study

introduces a self-adaptive GA to solve the system of equations of slope stability analysis. The applied procedure satisfies all conditions of equilibrium with a high degree of precision. Using the self-adaptive GA, all constraints of the problem are automatically handled into the optimization with no need for any penalty function on the objective function. For this purpose, a slope stability analyzer model is developed and coupled to the GA. The proposed model is applied against a benchmark example and the results are compared with the other conventional methods.

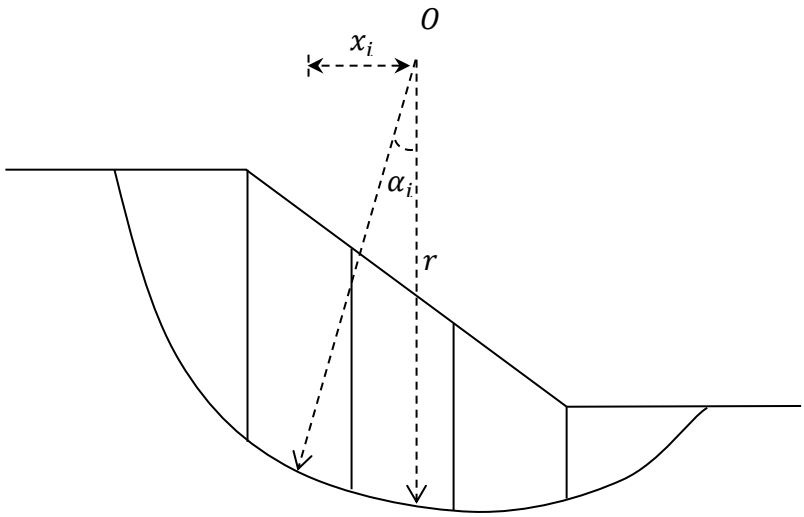


Figure 1. Sliding circular surface subdivided into vertical slices

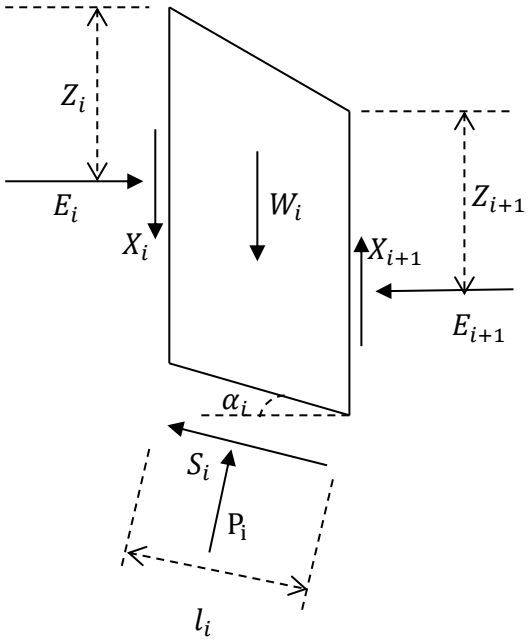


Figure 2. Free body diagram of a slice

2. Governing Equations

Geotechnical engineers frequently use the limit equilibrium methods of analysis when studying slope stability problems. For this purpose, the methods of slices are the most commonly used technique for the sake of their easiness in concept and implementation as well as ability to accommodate complex geometrics and variable soil and water pressure conditions [14].

Fig. 1 shows the potential sliding mass along a trial slip surface through a homogenous slope. The sliding mass is subdivided into a number of vertical slices. The free body diagram of a slice is illustrated in Fig. 2. The forces acting on the slice are its own weight W_i, slide forces, both having shear component X_i, and normal component E_i, and shear resistance S_i and the normal force P_i acting on the base of slice. Equating the moment of weight of the sliding mass with the moment of external forces acting on the slip surface about the center O of the slip circular surface yields:

$$\sum W_i \,.x_i = \sum S_i \,.r \tag{1}$$

where W_i is slice weight, S_i is shear forces in tangential direction to the base of the slice, and x_i and r are shown in Fig. 1. The relation between the shear strength of failure and equilibrium shear stress along the slide surface can be expressed as the following:

$$\tau = \frac{\tau_f}{F} \tag{2}$$

in which, F is the factor of safety and τ_f is the soil shear strength of failure calculated based on the Mohr-Clumb equation:

$$\tau_f = C' + \left(\frac{P_i}{l_i} - u_i\right).\tan\phi' \tag{3}$$

where C' is drained cohesion of the soil, $\phi'$is drained internal friction angle, l_i is the slice base length and u_i is the pore water pressure.

Combining equation 2 and 3 gives:

$$\tau = \frac{1}{F}[C' + \left(\frac{P_i}{l_i} - u_i\right).tan\,\phi'] \tag{4}$$

The vertical equilibrium for the slice i gives:

$$W_i + X_i - X_{i+1} = P_i \,.\cos\alpha_i + S_i \,.\sin\alpha_i \tag{5}$$

Rearranging for P_i yields:

$$P_i = (W_i + X_i - X_{i+1}) \,.\sec\alpha_i - S_i \,.\tan\alpha_i \tag{6}$$

Substituting the last expression in equation 4 and simplifying the result gives:

$$S_i = \frac{1}{F+\tan\alpha_i \,.\tan\phi'}\{C'.l_i + [(W_i + X_i - X_{i+1}).\sec\alpha_i - u_i \,.l_i].\tan\phi'\} \tag{7}$$

Hence, by substituting the last expression for S_i in equation 1 yields:

$$r.\sum \frac{\{C'.l_i+[(W_i+X_i-X_{i+1}).\sec\alpha_i-u_i.l_i].\tan\phi'\}}{F+\tan\alpha_i.\tan\phi'} = \sum r.W_i.\ \sin\alpha_i \quad (8)$$

The summation of the normal inter-slice forces should also be zero:

$$\sum(E_i - E_{i+1}) = 0 \quad (9)$$

Resolving the force acting on the slice in a tangential direction to the base of the slice results:

$$S_i = (E_i - E_{i+1}).\cos\alpha_i + (W_i + X_i - X_{i+1}).\sec\alpha_i \quad (10)$$

Therefor:

$$\sum(E_i - E_{i+1}) = \sum[S_i.\sec\alpha_i + (W_i + X_i - X_{i+1}).\tan\alpha_i] \quad (11)$$

Insertion of the value of S_i from equation 7 into equation 11 yields:

$$\sum\{\frac{C'.l_i+[(W_i+X_i-X_{i+1}).\sec\alpha_i-u_i.l_i].\tan\phi'}{F+\tan\alpha_i.\tan\phi'}.\sec\alpha_i - (W_i + X_i - X_{i+1}).\tan\alpha_i\} = 0 \quad (12)$$

Equations 8 and 12 are respectively the moment and force equilibrium equations. These equations should be solved to determine the unknowns X_i for every slice and the factor of safety F.

3. The optimization problem

The analysis of slope stability using the limit equilibrium methods is performed in two steps: First, the calculation of the factor of safety for a given slip surface and, second, a search for the critical slip surface with the minimum factor of safety of the slope. As earlier mentioned, the number of equations is less than the number of unknowns and the system of equations is thus indeterminate. Since, the process of finding the critical slip surface is linked to a technique for finding the minimum factor of safety; it could be possible to consider the process as an optimization problem. Here, equation 13 is considered as the optimization objective function. The acceptable bounds for the problem decision variables X_i, xc, yc, and r are considered as the problem constraints on the objective function. By minimizing the objective function subjected to the following inequality constraints, optimum values of the aforementioned decision variables are obtained.

Minimize F (safety factor) Subject to: (13)

$X_{i_l} \le X_i \le X_{i_u}\ \ i = 1,2,\dots,N$

$x_{c_l} \le x_c \le x_{c_u}$

$y_{c_l} \le y_c \le y_{c_u}$

$r_l \le r \le r_u$

$$(\text{Eq. } 8)^2 + (\text{Eq. } 12)^2 \le \varepsilon \quad (14)$$

where, subscriptions “l” and “u” indicate the lower and upper bounds of decision variables respectively and, ε is an acceptable tolerance to satisfy the compatibility of equations 8 and 12.

4. Self-Adaptive GA

To solve the above constrained mathematical programming model, a self-adaptive GA is developed as the following on the basis of a standard real GA:

1- An initial population with NP chromosomes is randomly generated within range $[0, 1]$. The chromosomes are decoded based on the upper and lower bounds of decision variables. Accordingly, each chromosome contains a set of feasible shear components (X_i) as well as the geometric parameters of slip surface (x_c, y_c, r). The slope stability analyzer program is run against each chromosome and the corresponding objective function (F) and the violation (V) of last constraint equation 14 are evaluated.

2- The binary tournament selection method [15] is used to select the parents. Through this step, the problem constraint (equation 14) is also handled so that, for each parent, two chromosomes x and y are randomly picked up from the population. x wins the tournament if one of the following conditions is met otherwise, y wins.

a. Both x and y are feasible but x has a greater objective function value.
b. Both x and y are infeasible but x has a smaller constraint violation.
c. x is feasible but y is not.

Accordingly, there is no need to penalize the objective function when a chromosome is infeasible. By using the above simple scheme, the GA can freely search into the problem decision space and gradually approach to the feasible regions.

The number of parents is considered to be half of the population size ($NP/2$). After all the required parents were selected, they are transferred to the mating pool to generate new offsprings.

3- The blend crossover method (BLX- α) proposed by Eshelman and Shaffer (1993) [16], is applied to each couple in the mating pool resulting in two children. When the crossover operator is applied to all couples, the population of children with NP size is created.

4- A few genes in the new population are mutated.

5- The children population is introduced to the slope stability analyzer program and F and V values in each new chromosome are evaluated.

6- The old and new populations are combined resulting in a population with 2NP size. The combined population is then divided into two subsets with respect to the feasibility and infeasibility of the chromosomes. The chromosomes with zero constraint violation are transferred to the feasible subset and the chromosomes with nonzero constraint violation are transferred to the infeasible subset. Let the size of feasible and infeasible subsets be respectively NF and NI so that, $NF + NI = 2NP$.

7- To form the new generation, we need to select the best NP chromosomes from 2NP chromosomes in the combined population. For this purpose, first the feasible subset is taken into account. If $NF \geq NP$, the feasible subset is sorted in descending order of the objective function value F. Then, the top NP chromosomes are selected as the next generation. Otherwise, if $NF < NP$, all NF chromosomes in the feasible subset are selected for the next generation. For the remaining $NP - NF$ chromosomes, the infeasible subset is sorted in ascending order of the constraint violation value V_{Rel_total}. Then, the top $NP - NF$ chromosomes in this subset are added to the selected feasible chromosomes. It is worth mentioning that, since the parents and children are combined

in each generation and the next generation is derived from both, the elitism is automatically preserved in the GA.

8- After the new generation was formed, the algorithm is repeated from step 2 until no further improvement is seen in the objective function.

5. Example

In this section, an illustrative example from the literature is adopted and analyzed using the proposed method. The geometry and soil parameters are presented in Fig 3. It is supposed that the center of the coordinate system is at point A. The factor of safety and slip surface geometric parameters are considered to be unknown.

The example is solved with 10 slices. Upper and lower bounds of decision variables are shown in Table 3. To solve the problem the GA population was decided 50 and the mutation ratio is 0.05. After about 200 generations the best results of the optimization were obtained as the following; $F = 2.35$; $x_c = 4.17\ m$; $y_c = 11.67\ m$ and $r = 9.4\ m$. For more investigations, the safety factors evaluated study in Table 4. Also, Table 5 in the previous studies are compared to the current presents the inter-slice shear forces obtained here it is compared to the previous works. Accordingly, concluded that the model has a good agreement with the previous well-known methods. Furthermore, the maximum constraint violation of $(Eq8)^2+(Eq12)^2$ is obtained 7E-06 which means that, both moment and force equilibrium equations have been precisely fulfilled through the applied model.

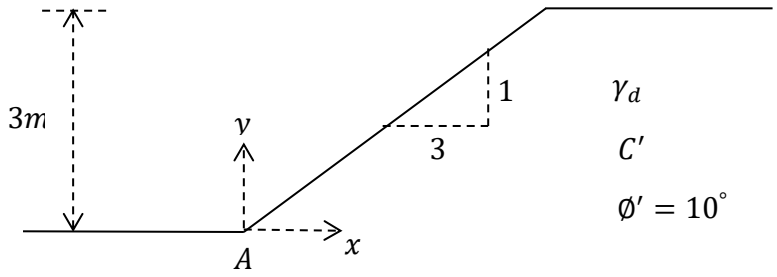


Figure 3. Geometry and soil parameters of example

Table 3. Upper and lower bounds of unknown values

	Lower limit	Upper limit
xc	0	15
yc	0	15
r	3	15
X1	1	10
X2	1	20
X3	1	22
X4	1	22
X5	1	25
X6	1	22
X7	1	20

X8	1	20
X9	1	10

Table 4. Factor of safety calculated by various methods

Bishop (1955)	Janbu (1956)	Morgenstern-Price (1965)	Samani-Meidani (2003)	Self-Adaptive GA (Present study)
2.394	2.125	2.391	2.437	2.350

Table 5. Inter-slice shear force calculated by different methods

	Constant-Interslice	Half-Sine	Corps of	Samani-Meidani	Self-Adaptive GA(Present Study)
X1	3.38	1.39	3.4	3	3.15
X2	7.27	5.49	7.3	7.4	7.84
X3	10.95	11.29	11	12.3	13.16
X4	13.54	16.28	13.6	19.7	20.82
X5	14.44	18.1	14.5	21.8	20.02
X6	14	17.04	14.06	22.5	20.68
X7	10.7	10.92	10.74	22.1	20.21
X8	7.35	6.12	7.4	21.5	19.63
X9	2.44	1.24	2.45	12	11.04

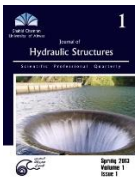
6. Conclusion

Design or evaluation of any embankment and slope to resist the destructive effects safely, requires to solve a complicated problem in the field of geotechnical engineering. The limit equilibrium methods are the most common technique for the slope stability analysis. The present study aimed at introducing an optimization framework based on optimization to solve the slope stability analysis problem. For this purpose, a self-adaptive GA was coupled to the Limit equilibrium and method of slices. Accordingly, the slope stability problem was transformed into a constrained optimization problem. Using the Self-Adaptive GA, there is no need to penalize the objective function when a chromosome violates the problem constraints. Through the proposed scheme, the GA can freely search into the problem decision space and gradually approach to the feasible regions where, the moment and force equilibrium equations are completely met. The method is applied to an example slope. The results for safety factor, inter-slice shear forces, coordinates of the slip circle center and radius were calculated. The results showed that model is in a good agreement with previous studies. The proposed procedure would be also applicable for dealing with problems with deferent soil layers, variable soil properties and having pore water pressure.

References

1. Duncan, J. M. 1996, "State of the art: Limit equilibrium and finite-element analysis of slopes", Journal of Geotechnical Engineering, vol. 122, no. 7, pp. 577-596.
2. Griffiths, D.V. and Lane, P.A., 1999. Slope stability analysis by finite elements. Geotechnique, 49(3), pp.387-403.
3. Griffiths, D.V. and Fenton, G.A., 2004. Probabilistic slope stability analysis by finite elements. Journal of Geotechnical and Geoenvironmental Engineering, 130(5), pp.507-518.
4. Griffiths, D.V. and Marquez, R.M., 2007. Three-dimensional slope stability analysis by elasto-plastic finite elements. Geotechnique, 57(6), pp.537-546
5. Fellenius, W. 1936, "Calculation of the stability of earth dams", Transactions, 2nd Congress on Large Dams, Washington, pp. 445-462.
6. Bishop, A. W. 1955, "The use of the slip circle in the stability analysis of slopes", Geotechnique,vol. 5, no. 1, pp. 7-17.
7. Janbu, N., Bjerrum, L., & Kjaernsli, B. 1956, "Soil mechanics applied to some engineering problems", Norwegian Geotechnical Institute Publication, vol. 16, pp. 1-93.
8. U.S.Army Corps of Engineers 1967, Stability of slopes and foundations, Engineering manual,Vicksburg, Miss. Whitman, R.V., and Bailey, W.A.
9. Spencer, E. 1967, "Method of analysis of stability of embankments assuming parallel inter-slice forces", Geotechnique, vol. 17, no. 1, pp. 11-26.
10. Morgenstern, N. R. & Price, V. E. 1965, "Analysis of stability of general slip surfaces",Geotechnique, vol. 15, no. 1, pp. 79-93.
11. Samani, Hossein M. V., and Meidani, M. (2003). “Slope Stability Analysis Using A Non-linear Optimization Technique.” International Journal of Engineering, Vol. 16, No. 2. pp. 147-156.
12. Sarma, S. K. 1979, "Stability analysis of embankments and slopes", American Society of Civil Engineers, Journal of the Geotechnical Engineering Division, vol. 105, no. 12, pp. 1511-1524.
13. Zhu, D. Y., Lee, C. F., & Jiang, H. D. 2003, "Generalized framework of limit equilibrium methods for slope stability analysis", Geotechnique, vol. 53, no. 4, pp. 377-395.
14. Terzaghi. K. and Peck. R. B. 1967.S oil mechanics i n engineering practice. (2nd ed.), John Wiley and Sons lnc. New York. N.Y.Deb,
15. K.,Pratap,A.,Agarwal.,S.,Meyarivan,T.,2002.A fast and elitist multi-objective genetic algorithm:NSGA-II.IEEETrans.Evolut.Comput. 6(2), 182–197.
16. Eshelman, L.J., Shaffer,D.J., 1993. Real-coded genetic algorithms and interval schemata.In:Whitley,D.L.(Ed.),FoundationsofGeneticAlgorithms2. Morgan Kaufman, SanMateo,CA,pp.187–202

Journal of Hydraulic Structures
***J. Hydraul. Struct.*, 2016; 2(1):58-70**
DOI: 10.22055/jhs.2016.12651



Calculation of Leakage in Water Supply Network Based on Blind Source Separation Theory

JinliangGao[1a]
ShihuaQi[1]
Jun Nan[1]
Juanjuan Li[1]

Abstract

The economic and environmental losses due to serious leakage in the urban water supply network have increased the effort to control the water leakage. However, current methods for leakage estimation are inaccurate leading to the development of ineffective leakage controls. Therefore, this study proposes a method based on the blind source separation theory (BSS) to calculate the leakage of water supply network. The method uses fast independent component analysis (FastICA) algorithm to separate flow signal of laboratory and practical measuring area, adopts trend similarity to solve the uncertainty of separation sequence to get hourly change curve of user usage and physical leakage, and embeds the leakage model into amplitude optimization model to solve amplitude uncertainty to obtain physical leakage value. The study found that the estimation of leakage level using the blind source separation is reasonably accurate and facilitates the identification of the subsequent reduction in water leakage. This can provide scientific evidence for leakage reduction and the investment of pressure relief devices in the next stage.

Keywords: blind source separation theory (BSS); fast independent component analysis (FastICA); leakage simulation; water consumption; water supply network (WSN); water leakage.

Received: 24 February 2016; Accepted: 2 July 2016

1. Introduction

Leakage in water supply network is a general problem in water supply enterprises and different measures such as Minimum Night Flow (Tabesh 2009), "Water Balance" (AWWA 1999; Winarni 2009), Network Leakage Hydraulic Model (Almandoz, et al. 2005) and Regional

[1] Harbin Institute of Technology, No. 73 Huanghe Rd, Harbin, 150090, P.R. China
[a] Corresponding author; JinliangGao. Tel.: 0086-13936477968; fax: 0086-451-82311926.
E-mail address:gjl@hit.edu.cn

Leakage Estimation (Buchberger & Nadimpalli 2004)have been adopted to calculate the physical leakage. However, the methods are generally ineffective due to the use of inaccurate analysis of regional leakage quantity and sequential characteristics.

Minimum Night Flow requires data collection at night with no water consumption or during the hour with minimum water consumption (Tabesh 2009), and significant amount of manpower and materials. Consequently, the method requires significant disruption to the regional water supply and has high uncertainty in the actual regional water consumption estimation. Similarly, "Water Balance", proposed by the International Water Association (IWA), calculates the amount of leakage based on the difference between the production and consumption, which needs to install many flow meter or water meter in the branch of water network (AWWA 1999). It also has several drawbacks such as inaccurate customer metering, use of estimated values for unbilled or unmetered consumption, need for the installation of significant amount meters (Winarni 2009). Further, the Water Balance is effective for accumulated leakage and unsuitable to analyze the hourly variation leakage. Similarly, the Network Leakage Hydraulic Model produces subjective results since it primarily depends on the experience (Almandoz, et al. 2005), while, the Regional Leakage Estimation does not predict the real time leakage (Buchberger & Nadimpalli 2004). Therefore, it is necessary to develop alternative methods that can estimate the actual water leakage accurately. One such alternative method for water leakage estimation is the Blind Source Separation(BSS) (Comon & Jutten 2010), which is used for processing signals that have unknown source similar to water consumption and leakage amount. Overall, this study proposes an algorithm to obtain the curve of water leakage changes with time, which is the foundation for reducing water leakage through adjusting hourly pressure of the inlet of water supply network (WSN).

2. Methods

2.1. BBS Theory

BSS, which is a powerful signal processing technology developed in the 1980s, is a combination of artificial neural network, medical signal processing, statistical signal processing and information theory (Comon & Jutten 2010). BSS detects the sensor signal from a multi-input-and-output nonlinear dynamic system, and consequently finds an inverse system to estimate and reconstitute the original signal source (Comon & Jutten 2010). In this process, the original signal and the method that the source signal used to obtain the observation signal are unknown.

2.2 Fast independent component analysis (FastICA)

Comon (1994) suggested the core algorithm, namely independent component analysis (ICA),for blind source separation. It synchronously observes overlapping signals in multi channels and separates the observation signals into independent parts to estimate the source signal. Fast independent component analysis (FastICA) is a high-speed algorithm based on ICA proposed by Hyvärinen (Hyvärinen1999; Hyvärinen & Oja 2000). FastICA has fast rate of convergence, and is appropriate for processing non-Gaussian data. It can extract an independent part from the observation signals every time.

2.3 Evaluation index for BSS

The performance of FastICA can be evaluated by assessing two criteria, namely similarity coefficient and performance index. The similarity coefficient was taken as the criterion to

evaluate the similarity between separated and real water consumption leakage.

Similarity coefficient between separated consumption and leakage in different operating conditions $s'(t) = [s'_1(t), s'_2(t)]^T$ and the real consumption and leakage $s(t) = [s_1(t), s_2(t)]^T$ was used as an assessment criterion of leakage separation, as shown in equation (1):

$$\xi_{y,s} = \frac{\left|\sum_{t=1}^{T}[s(t) - E\{s(t)\}] \cdot [y(t) - E\{y(t)\}]\right|}{\sqrt{\sum_{t=1}^{T}[s(t) - E\{s(t)\}]^2 \cdot \sum_{t=1}^{T}[y(t) - E\{y(t)\}]^2}} \tag{1}$$

where set y and s 1 and 2, respectively. y=1 represents real water consumption, while y=2 represents real leakage. Similarly, s =1 represents separated water consumption, while s =2 represents separated leakage. When ξ_{11} is close to 1, the real water consumption approaches the separated water consumption value, whereas the real leakage approaches the separated value of leakage when ξ_{22} is approximately 1.

2.4 FastICA for BSS

The signal noise was present from the flow meter in water supply network due to the interference of the external environment. Therefore, preprocessing of the signals was used to guarantee the precision of the signal separation. In this study, FastICA was used to apply blind source separation and the preprocessing included the following:

- The physical leakage was obtained from the total flow of water supply network and the mathematical model was built according to the blind source separation theory, as shown in equation (2):

$$X = AS \tag{2}$$

Where X is the observation signal, A is the hybrid matrix of the source signals.

- Tabesh, et al. (2002) suggested that the node flow points are actual water consumption and the physical leakage. The model of regional water supply network BSS can be consequently subdivided as shown in equation (3):

$$X = \begin{bmatrix} x_1 \\ x_2 \end{bmatrix} = \begin{bmatrix} Q_1 \\ Q_2 \end{bmatrix}, S = \begin{bmatrix} s_1 \\ s_2 \end{bmatrix} = \begin{bmatrix} q_y \\ q_l \end{bmatrix}, A = \begin{bmatrix} a_{11} & a_{12} \\ a_{21} & a_{22} \end{bmatrix} \tag{3}$$

where Q_1 is regional total input volume and Q_2 is main branch volume, q_y and q_l are the actual user water consumption and physical leakage. The total water supply was obtained from the combination of the actual user water consumption and physical leakage. The physical leakage can be separated from the WSN using the FastICA algorithm.

- Whitening was used before separation, because they completely lost connection after whitening, as shown in equation (4):

$$\bar{X}(t) = Q_w X(t) \tag{4}$$

where Q_w is the whitening matrix.

FastICA algorithm, also known as fixed point algorithm, is a non-Gaussian maximization algorithm. It searches the non-Gaussian maximum using the fixed-point iteration theory. This algorithm adopts the Newton iteration method to batch the observational variable at a large number of sampling sites. It uses maximized negative entropy as objective function and processes an independent element from the observation signals every time. The flowchart for FastICA is illustrated in Fig. 1.

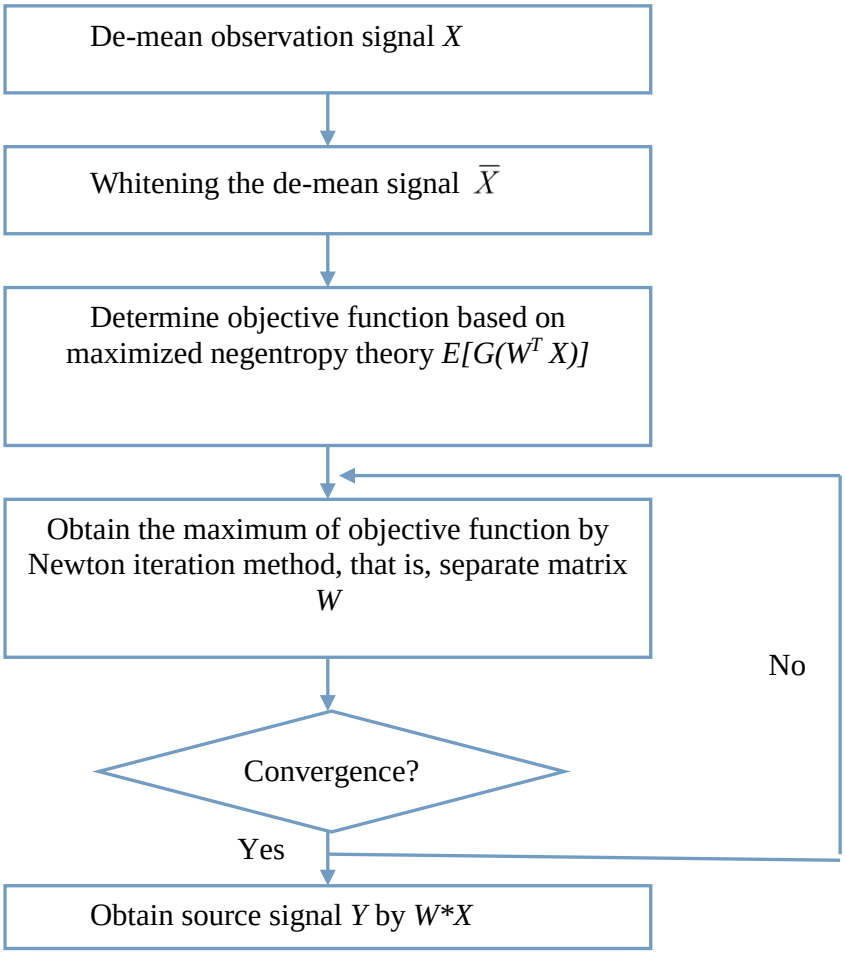


Fig. 1. Processing steps of FastICA

BSS Programming was established by using relevant MATLAB toolbox (Mathworks, 2014).

2.5 Amplitude solution

The uncertainty of the signal obtained by blind source separation contains sequential uncertainty and amplitude uncertainty (Tong 1991). Sequential uncertainty restricts the ability to separate the physical leakage from different components, while the amplitude uncertainty limits the ability to obtain the actual leakage and to analyze the dynamic change in the physical leakage.

In this study, trend similarity was adopted to solve uncertainty of separation sequence. Over determined systems were established to calculate source signal mean and variance based on the law of mass conservation, and solved by the genetic algorithm. The amplitude uncertainty was solved through converting the amplitude into significant physical leakage. The specific solutions of amplitude uncertainty include: embedding the leakage model into amplitude optimization model; setting average pressure for the laboratory pipe network; networking total flow and separated water consumption as given value; setting leakage coefficient and leakage index as unknown quantities of leakage model; setting amplitude translation amount and amplitude proportion coefficient as unknown quantities of the water model; establishing the water balance equation and using multiple iterative operation of genetic algorithm optimization to obtain leakage coefficient, leakage index, amplitude translation and amplitude ratio; and sequentially solving the problem of water consumption amplitude. In this study, the Genetic Algorithm consisted of 4 independent variables, population of 500, crossover rate of 0.8 and mutational rate of 0.1. Water balance equation is shown in equation (5):

$$\begin{cases} Q_i = Q_{y_i} + Q_{l_i} \\ Q_{y_i} = (a_i + x)y \;\; i = 1,2,3\ldots12 \\ Q_{l_i} = k_i P_i^{\beta} \end{cases} \tag{5}$$

where a_i is the mean of separated water consumption in each operating condition, x is the translation of separated water consumption, y is the amplitude proportionality coefficient of separated water consumption(L/s), P_i is the average water head of pipe network(mH_2O), Q_i is the total flow in pipe network(L/s), Q_{y_i} is the separated water consumption of pipe network(L/s) and Q_{l_i} is the actual leakage of pipe network(L/s).

2.6 Laboratory based case study

An experimental platform of water supply network leakage (Fig. 2) was established to apply blind source separation for the water supply network leakage separation. This platform was able to simulate different pipe network scenarios by controlling the speed of the pumps and on-off control of the valves such as single water source loop pipe network leakage simulation, single water source ring combination of pipeline leakage simulation and multi- water sources loop pipe network leakage simulation. The water supply pipes were setup vertically to simulate the real pipes with different heights. A control cabinet was used to control the water pumps, and 3 horizontal multi-stage speed centrifugal pumps were used to supply water for the pipe network. Additionally, a water tank was used as the water supply source and backwater device. The pipes used in the water supply network were made up of Unplasticised Polyvinyl Chloride (UPVC) and an online pressure gauge was installed in the network to detect the pipe pressure.

Furthermore, a turbine flow meter was used at the outlet of the pump.



Fig. 2. Experimental platform of Leakage Separation of Water Supply Network

Water consuming nodes and leakage points are shown in Fig.3. There network consisted of 4 nodes in the water supply network and 3 water meters at every node to quantify the water consumption and the leakage. B, D, F and H represent users, while A, C, E and G represent leaking points. The leaking points were controlled by on-off controls at valves A, C, E and G. The leakage can be determined by controlling the level of valves A, C, E and G.

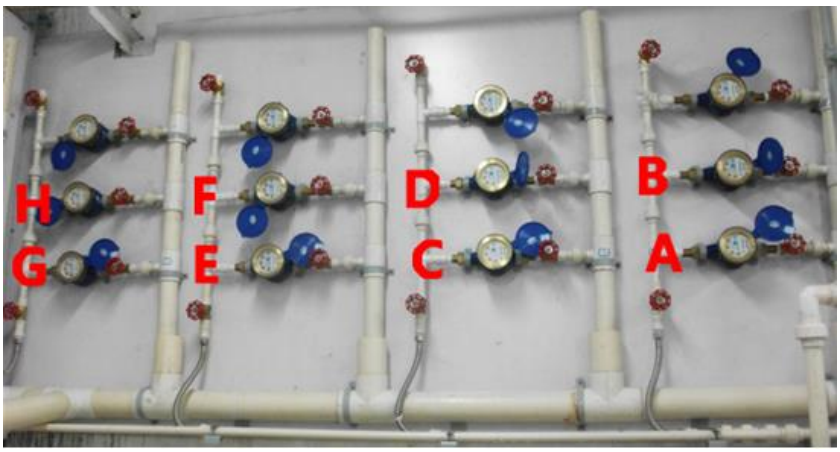


Fig. 3. Water Consuming Nodes and Leaking Points

Considering the features of a typical water supply network, the leakage separation of network was set up in laboratory. The Supervisory Control And Data Acquisition (SCADA) system data were considered as the observation signals, while the real water consumption and physical leakage were considered as the source signals. While the level of valves A, C, E and G were kept constant, the water consumption model was changed by altering the level of valves B,

D, F and H. However, the frequencies of pumps and the flow rates were not changed. Additionally, the real water consumption and leakage were recorded, while the amount of leakage separated by applying BSS. The separation performance was evaluated by comparing the separated data with the real water consumption and leakage.

In a multi-water source loop pipe network leakage, the SCADA online data was used to record the flow observation signals of 9648 sets in a network under 14 operating conditions, as shown in Fig. 4.

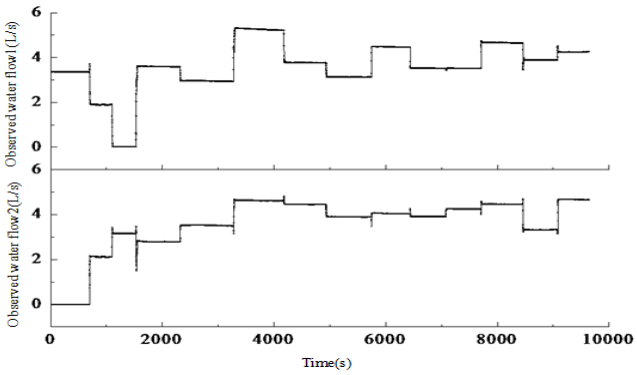


Fig. 4. Observation Signals (1. regional total input volume, 2. main branch volume) of Flow Meters

The separated signals of FastICA are shown in Fig. 5.

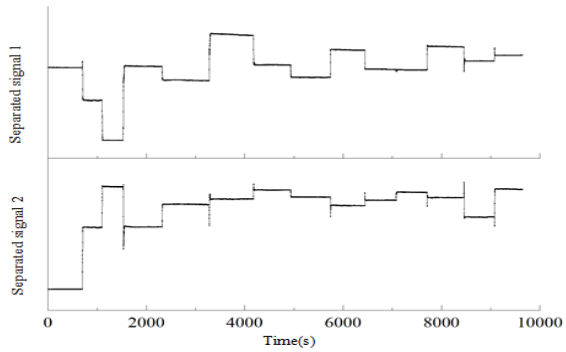


Fig. 5. Variation Trend of Separated Signals

As can be seen from Fig.5, the variation trend that separated signal 1, which is regarded as separation value for water consumption, is similar with the real water consumption. Multiple iterative operation of GA optimization was used to obtain the amplitude translation and proportionality coefficient in order to investigate the amplitude uncertainty. Consequently, the simulated water consumption of multi-water source loop network was obtained using the genetic algorithm optimization, while the simulated physical leakage was calculated from the difference between the production and consumption. The relative error between the simulated and real water consumption and leakage is shown in Table 1.

Table 1. Simulated Water Consumption and Leakage with BSS

Operating Condition	Real Leakage (L/s)	Simulated Leakage (L/s)	Relative Error (%)	Real Water Consumption (L/s)	Simulated Water Consumption (L/s)	Relative Error (%)
1	0.880	0.742	15.71	0.000	0.246	—
2	1.189	1.085	8.69	0.000	0.103	—
3	0.844	0.779	7.70	0.000	0.165	—
4	0.914	0.864	5.47	0.954	1.004	5.25
5	0.922	0.856	7.08	0.991	1.057	6.58
6	0.573	0.626	9.13	2.442	2.289	6.24
7	0.494	0.526	6.61	1.966	1.903	3.19
8	0.819	0.771	5.89	1.264	1.313	3.82
9	0.980	1.015	3.54	1.557	1.522	2.23
10	0.911	0.911	0.01	1.308	1.308	0.01
11	0.733	0.797	8.67	1.566	1.503	4.06
12	0.883	0.983	11.35	1.797	1.696	5.58
13	0.619	0.639	3.27	1.509	1.489	1.34
14	0.715	0.791	10.52	1.947	1.872	3.87
Total Flow(L/s)	11.476	11.385	0.80	17.301	17.471	0.98

From Table 1, it can be seen that the simulated water consumption fluctuates around the real water consumption, with a relative error ranging from0.01% to 6.58%. The simulated leakage fluctuates around the real leakage, with a relative error ranging from0.01% to 15.71%. The simulated total leakage error is 0.98%, while the simulated water consumption error is 0.8%.

The similarity coefficient for the real and simulated leakage is 0.876, while the similarity coefficient for real and simulated water consumption is 0.929. This suggests that the separation performance is fairly satisfied.

3. Case study

A secondary metering area in the urban water supply network of a southern-China coastal city was used as the case study. The urban water supply system in the area had SCADA and Geographic Information System (GIS) systems and had about 10 km of total length of the water supply network. There were inlet flow meters (A and B), a neighborhood inlet flow meter (C) and three pressure monitoring points (P1, P2 and P3) as shown in Fig. 6.

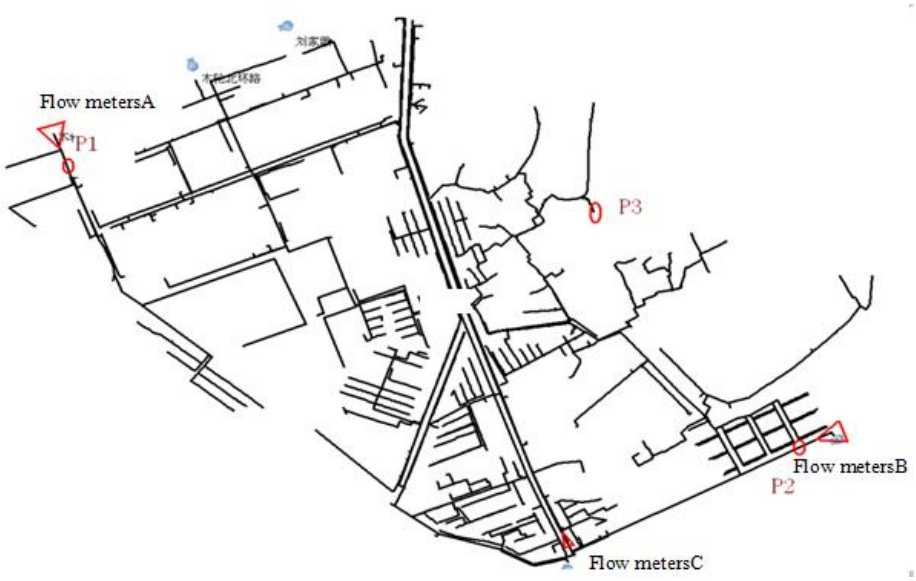


Fig. 6. Network Topology of Metering Area

There are multi-water source and branch-loop combined water supply networks in this area. The data for three flow meters on date X can be obtained and shown in Fig.7(a), while the pressure data is plotted in Fig. 7(b).

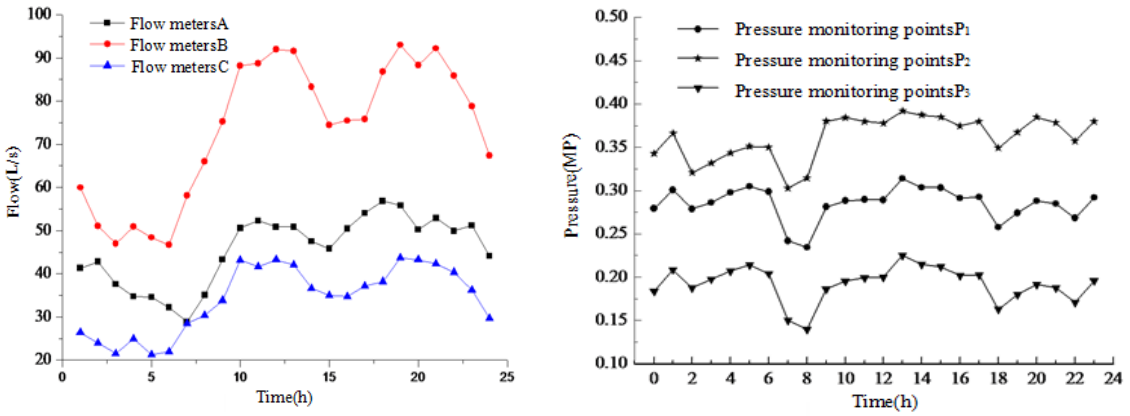


Fig. 7. a. Flow meter measured data, b. Pressure data

According to the laboratory scale leakage separation method study, the two flow observation signals were the inputs, where the sum of flow through meters A and B was one input, while the amount of flow through meter C was another. By using FastICA, the variation trend shown in Fig. 8 can be obtained.

The water balance equation was developed based on the energy conservation principles in order to eliminate the uncertainty in the amplitude of separated water consumption. Genetic

optimization leads to the simulated water consumption and simulated leakage, as shown in Table 2.

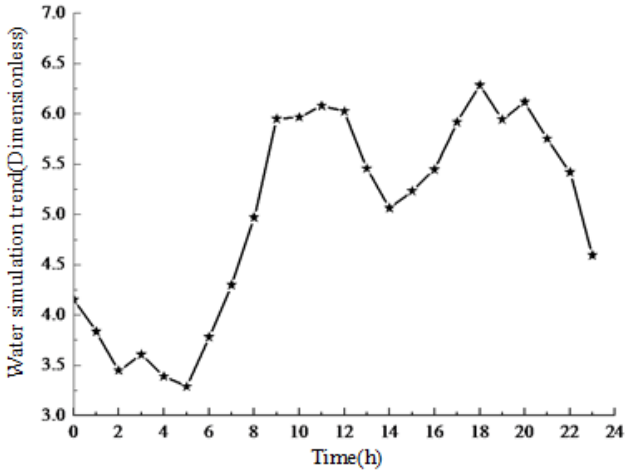


Fig. 8. Variation trend of separated water consumption

Table 2. Simulated Water Consumption and Leakage in 24 hours

Time(h)	1	2	3	4	5	6
Simulated Water Consumption(l/s)	83.214	75.908	67.053	70.669	65.700	63.366
Simulated Leakage(l/s)	16.033	16.814	15.900	16.228	16.578	16.808
Time(h)	7	8	9	10	11	12
Simulated Water Consumption (l/s)	74.689	86.536	102.011	124.556	124.958	127.578
Simulated Leakage (l/s)	16.589	14.753	14.600	16.400	16.647	16.681
Time(h)	13	14	15	16	17	18
Simulated Water Consumption (l/s)	126.317	113.261	104.172	108.069	112.978	123.864
Simulated Leakage (l/s)	16.669	17.389	17.106	17.039	16.692	16.758
Time(h)	19	20	21	22	23	24
Simulated Water Consumption (l/s)	132.267	124.472	128.453	119.994	112.350	93.383
Simulated Leakage (l/s)	15.531	16.131	16.575	16.433	15.828	16.642

The actual total volume of water supply on date X in this metering area was 10292.29 m^3, and the simulated leakage volume after blind source separation is 1414.16 m^3. Thus, the simulated leakage percentage was 13.74% of the actual water supply volume. The water audit analysis showed that the daily production and marketing difference on date X was 15.68%. Since 80% of the production and marketing difference is leakage, the leakage percentage was 12.54%. The error between the leakage percentage from FastICA and the one shown by water audit was only 1.2%. Therefore, it can be concluded that calculating the leakage percentage using separating leakage with FastICA algorithm is reliable.

4. Results

This study applied BSS for both laboratory water supply network and regional water supply network. In the laboratory leakage separation experiment, the relative error range between simulated and real leakage is only 0.01%~15.71%, while the error in simulated total leakage is 0.98%.Furthermore, the similarity coefficient between simulated and real leakage is 0.876. In the regional water supply network, the error between calculated leakage rate and the rate given by the water audit is only 1.2%. A significant portion of the data was obtained by laboratory leakage separation experiment, which was limited to topology of WSN, node flow and pressure control. The control mode of these experiments was achieved by adjusting water valves and pump speeds. Therefore, the reliability of the results needs further investigation using different experimental water network and different conditions. In the actual field test with traditional methods, it is difficult to detect hourly amount of water leakage resulting in unreliable and inaccurate test results. The leakage amount in the main branch of WSN needs to be measured in Minimum Night Flow. However, such measurement is difficult since it requires the installation of a significant number of water meters, especially in complex loop WSN in china. Consequently, the measured flow data were all off-line with low accuracy. In contrast, real-time monitoring data is reliable and accurate. However, establishing the remote communication is a major issue. In addition, the installation of excessive water meters would increase the experimental error.

Furthermore, the water leakage obtained from the pressure reducing experiment is unreliable, since the changing pressure would have affected water consumption. Similarly, node leakage model only considers single node leakage rather than total leakage of each node of regional WSN. However, in this study, the estimation of total leakage of regional WSN was calculated based on BSS with the measurement of two water volume (usually is regional total input volume and main branch volume) and one network average pressure.

5. Discussion

It is worthy to note that the results obtained in this study were relatively more accurate compared to the results obtained using the traditional methods. Water consumption and node water leakage has different characteristics of pressure, trend, requirement and output. The measurement value of two water volume and one network average pressure were interacted results of water consumption, node water leakage, pipeline head loss and node pressure. The leakage coefficient and index can be obtained based on the node leakage model using measured volume of regional water leakage, then the coefficient and index can be used to adjust pressure and control leakage.

This study proposed that system input volume consisted of two variation of water amount, namely water consumption and water leakage. Therefore, the water leakage curves were obtained each hour using FastICA. Kalman Filter Algorithm, Wavelet Analysis Algorithm or any other algorithm are recommended to separate water leakage from system input volume for further study, and compare the efficiency and accuracy of each algorithm.

6. Conclusion

In water supply network, linear relationship is difficult to obtain. This study investigated a method that uses BSS as a substitute for nonlinear relationship. BSS can only provide the trend of time, while the obtaining the trend of amplitude was not possible. Calculation of leakage in WSN based on BSS is simulated in both laboratory and field. Hourly water leakage of WSN can

be simply obtained based on BSS using only two water volume (usually is regional input volume and main branch volume) and one network average pressure. The results concluded that the BSS is a relatively accurate and effective method to determine the leakage and to control the network leakage. BSS also can distribute all leakage volume to each working condition and can provide accurate data support of leakage characteristics analysis and leakage control hydraulic model. This can provide solid support for leakage reduction purposes and for the investment in pressure relief devices in the next stage.

7. Acknowledgement

This research was supported by the National Water Pollution Control and Treatment Science and Technology Major Project (2014ZX07405002C), National Natural Science Foundation of China (51278148) and The Union Project of Industry-study-research of Guangdong Provincial Department of Education (2011A090200040). The partial paper are from WDSA2014 “Study on Leakage Rate in Water Distribution Network Using Fast Independent Component Analysis”.

Reference

1. Almandoz, J., Cabrera, E., Arregui, F., et al. 2005 Leakage assessment through water distribution network simulation. *Journal of water resources planning and management*. 131(6), 458-466.
2. American Water Works Association , 1999 2nd edition, Manual M36, *Water audits and leak detection*, AWWA.
3. Buchberger, S. & Nadimpali, G. 2004 Leak estimation in water distribution system by statistical analysis of flow readings. *J. Water Resour. Plann. and Manage*. 130(4), 321-329.
4. Comon, P. 1994 Independent component analysis, a new concept? *J. Signal Processing*. 36(3), 287-314.
5. Comon, P. & Jutten, C. (Eds.). 2010 Handbook of blind source separation: Independent com ponent analysis and applications. Academic press.
6. Gao, J., Qi, S. & Wu, W. 2014 Study on leakage rate in water distribution network using fast independent component analysis. *WDSA 2014, Bari, Italy: Procedia Engineering.* 89(2014), 934-941.
7. Hyvärinen, A. 1999 Fast and robust fixed-point algorithms for independent component analysis. *J. Neural Networks.* 10(3), 626-634.
8. Hyvärinen, A. & Oja, E. 2000 Independent component analysis: algorithms and applications. *J. Neural Networks.* 13(4-5), 411-430.
9. Mathworks. 2014 < http://www.mathworks.com/matlabcentral/fileexchange/47069-convolutive-bss > (Accessed 04 May 2015)
10. Rossman, L. 2000 *EPANET User's Manual*. United States Environmental Protection Agency, Cincinnati, U.S.A.
11. Tabesh, M., Tanyimboh, T.T. & Burrows, R. 2002 Head driven simulation of water supply networks. *IJE Transactions A: Basics.* 15(1), 11-22.
12. Tabesh, M., Asadiyani, A.H. & Burrows, R. 2009 An Integrated Model to Evaluate Losses in Water Distribution Systems. *Water Resources Management.* 23(3), 477-492

13. Tong, L., Liu, R. & Soon, V.C. 1991 Inderminacy and identifiability of blind identification. *IEEE Transactions on Circuits and Systems*. 38(5), 499-509.
14. Winarni, W. 2009 Infrastructure Leakage Index (ILI) as water losses indicator. *Civil Engineering Dimension.* 11(2), 126-134.

Journal of
Hydraulic Structures
Scientific Professional Journal

Contents

Volume 2 - Issue 1 - 2016

Riprap sizing for scour protection at river confluence (1-11)
E. G. Adivi, M. S. Bajestan, J Kermannezhad

Experimental Investigation of Rill Creating Hydraulic Conditions in the Marl Rangelands in a Tilting Flume (12-26)
A. Zoratipour, H. Azadi

Experimentally determination of discharge coefficients of Ogee spillway under axial arc condition with convergent lateral walls (27-33)
J. S. Kazemi, M. Saneie, M. AzhdaryMoghaddam

Shape Optimization of an abrupt contraction using numerical streamlining (34-47)
R. Yousefian, S. F. Saghravani

Slope Stability Analysis Using a Self-Adaptive Genetic Algorithm (48-57)
A.H. Ayati, H.M.V. Samani, A. Haghighi

Calculation of Leakage in Water Supply Network Based on Blind Source Separation Theory (58-70)
J. Gao, S. Qi, J. Nan, J. Li

Address :
Engineering Faculty, Shahid Chamran University of Ahvaz
Phone: +986113330011 , +986113337010
Website: jhs.scu.ac.ir
Email: jhs@scu.ac.ir
Ahvaz, Khouzestan Province, Iran